





Equation of state modeling with pseudoatom molecular dynamics

A. A. Ovechkin ^{1,*}, P. A. Loboda ^{1,2}, A. L. Falkov ¹ and P. A. Sapozhnikov ¹

¹Russian Federal Nuclear Center, Zababakhin All-Russian Research Institute of Technical Physics (RFNC-VNIITF), Snezhinsk, Chelyabinsk region 456770, Russia

²National Research Nuclear University, Moscow Engineering Physics Institute (MEPhI), Moscow 115409, Russia



(Received 1 February 2021; accepted 28 April 2021; published 14 May 2021)

Using a modified version of the pseudoatom molecular-dynamics approach, the silicon and oxygen equations of state were generated and then employed to construct the equation of state of silicon dioxide. The results are supported by the close agreement with *ab initio* simulations of the silicon pressure and experimental shock Hugoniot of silicon dioxide. Ion thermal contributions to thermodynamic functions provided by the PAMD simulations are compared to their counterparts obtained with the one-component plasma and charged-hard-sphere approximations.

DOI: [10.1103/PhysRevE.103.053206](https://doi.org/10.1103/PhysRevE.103.053206)

I. INTRODUCTION

Many studies on high-energy-density physics involving the excitation of matter with intense energy fluxes come across the phase-space region characterized by comparable values of kinetic and potential energies of electrons and ions along with the partial electron degeneracy—the warm dense matter (WDM) domain [1]. At the same time, available experimental data on thermodynamical and optical properties of WDM are rather limited and frequently have insufficient accuracy, thus driving a need for reliable nonempirical theoretical methods. In principle, at WDM temperatures (less than or around the Fermi energy E_F) and material densities (of the order of normal density) most accurate results are provided by the *ab initio* quantum-molecular-dynamics (QMD) simulations [2]. However, the QMD range of applicability is rather limited due to the dramatic increase of computational cost at temperatures $T \gtrsim E_F$ and the constraints of the pseudopotential approach, employed in QMD simulations, brought on by disregard of core-electron thermal excitation or pressure ionization at sufficiently high temperatures or densities. Therefore, to obtain a wide-range equation of state (EOS), one also needs to use other complementary methods being valid in the parameter domains partially overlapping with the QMD applicability range. As an example, some wide-range EOS [3,4] were successfully generated by combining the QMD results with the simulation data obtained by using another *ab initio* method—many-body path integral Monte Carlo (PIMC) method [5–7]. Such simulations are, however, very time-consuming and are currently feasible only for the low- and mid- Z elements.

Wide-range EOS may be constructed by matching the calculated data obtained with QMD and single-center average-atom (AA) models [8–24]. Though such techniques hold much favour, the implementation of those faces the long-standing problem of proper account of the ion thermal contribution in the context of the AA model [8,9,20,25] that should be addressed with some additional approximations

invoked. This is generally done by using the models initially formulated for solids [8,26,27] and then extrapolated to liquids so as to recover the correct ideal-plasma limit at high temperatures. An alternative approach utilizes the known expressions for thermodynamic functions of some idealized reference systems (see Sec. II). However, both approaches cannot provide consistent and accurate treatment of ion correlations in real warm and moderately hot plasmas. Therefore, their use at plasma temperatures and densities high enough to make QMD calculations impracticable leads to considerable uncertainties in the AA-based EOS data due to a still sufficiently strong interparticle coupling. So one needs a formulation suitable for making EOS calculations at temperatures and densities no longer feasible for conventional QMD simulations along with an appropriate treatment of strong interparticle correlations and the absence of restrictions common to AA models. In principle, all these conditions are met if one employs semiclassical formulation of QMD known as orbital-free molecular dynamics [28–30], except that its accuracy is constrained by the inability to represent quantum shell-structure effects. We have therefore implemented an alternative promising approach of pseudoatom molecular dynamics (PAMD) [31,32] briefly discussed in Secs. II and III. In Sec. III we describe an improvement to the original method to calculate thermodynamic functions in the context of the PAMD simulations [32]. Section IV deals with various techniques to classify electrons into the bound and free ones that affect both PAMD-simulated data and ion contributions to AA thermodynamic functions. Sections V and VI present comparisons of the results obtained to other *ab initio* simulations and experimental data. Using the PAMD-simulated data, in Sec. V we also examine various approximations to allow for the ion thermal contribution to the AA-based equations of state.

II. ION THERMAL CONTRIBUTION TO THE EOS

Average-atom models cited above have been successfully used for years to characterize thermodynamic properties of

*ovechkin.an@mail.ru

high-temperature plasmas under a wide range of temperature and density conditions. The models are, however, subject to certain constraints limiting their applicability. Specifically, commonly known and most serious constraint, as mentioned above, is brought on by the impossibility to consistently treat ion correlations in the AA picture with only a few exceptions represented, e.g., by the Starrett and Saumon [21,22] or the SCAALP [16,19] models.

Consequently, a realistic ion-ion pair correlation function cannot be generally found and simple step function is usually employed instead:

$$g(r) = \theta(r - r_0). \quad (1)$$

Here $\theta(x)$ is the Heaviside function, $r_0 = [3/(4\pi n_i)]^{1/3}$ is the atomic-cell radius with $n_i = \rho N_A/A$ being the average ion density expressed in terms of the material density ρ , Avogadro constant N_A , and atomic weight A (in g/mole). The use of this simplification would lead to inaccuracies of the calculated thermodynamic functions being especially significant in the case of sufficiently strong Coulomb coupling. Therefore, it is a common practice to add ion-correlation corrections to the ideal-gas ion contributions to the AA thermodynamic functions. To evaluate those, a real electron-ion system is usually mapped to some idealized reference system being characterized by a small number of parameters and enabling one to explicitly derive the corrections discussed. As an example, one can refer to the one-component plasma (OCP) [33]—a widely used reference system of pointlike ions immersed in a uniform neutralizing background. Another example is the charged-hard-sphere (CHS) system [9,34–36] differing from the OCP by the account of finite ion size. The OCP thermodynamic functions are controlled by only one dimensionless parameter of ion-ion Coulomb coupling Γ being expressible in terms of the mean ion charge Z_0 that may be found with an AA model [37]:

$$\Gamma = Z_0^2/(r_0 T). \quad (2)$$

The internal energy (per one atom) and pressure with the OCP ion-correlation corrections may be written as (see, e.g., Ref. [9])

$$E = E_e + T[3/2 + \delta E_i^{\text{OCP}}(\Gamma) - \delta E_0^{\text{OCP}}(\Gamma)], \quad (3)$$

$$P = P_e + T n_i \{1 + [\delta E_i^{\text{OCP}}(\Gamma) - \delta E_0^{\text{OCP}}(\Gamma)]/3\}, \quad (4)$$

where E_e and P_e are the AA electron components of internal energy and pressure, respectively, and the term $T \delta E_0^{\text{OCP}}(\Gamma) \approx -0.9T \Gamma$ is extracted since its AA counterpart (which, unlike $T \delta E_i^{\text{OCP}}$, allows for the electron-density nonuniformity) has already been included in E_e .

In addition to the ion-ion Coulomb coupling parameter, the CHS system also employs an effective parameter of packing fraction η defined as the ratio of the volume occupied by plasma ions to the total plasma volume:

$$\eta = (r_*/r_0)^3, \quad (5)$$

where r_* is an effective radius of the ion core. We evaluate the latter one assuming that r_* is equal to a distance at which the electrostatic field strength in average atom coincides with

the field strength of a pointlike charge of the value Z_0 [9]:

$$4\pi \int_0^{r_*} n_e(r) r^2 dr = Z - Z_0 \quad (6)$$

with $n_e(r)$ being the electron density. To avoid nonphysically large values of r_* at $Z_0 \approx 0$ (at low temperatures and material densities), ion-core radius is additionally majorized by the mean radius of the outermost occupied orbital of the relevant neutral atom. In the CHS approximation, the expression for the internal energy (3) remains unchanged while the pressure receives an additional hard-sphere-model correction $T n_i \delta P_i^{\text{HS}}(\eta)$ [38].

The problem with the use of the OCP or CHS ion thermal contributions for the AA-based equations of state is, however, that the relevant reference systems are too idealized and exhibit a pronounced sensitivity to the techniques of evaluating reference-system parameters, especially the packing fraction. The PAMD approach is free of such shortcomings, since the effects due to ion correlations are directly modeled in PAMD using classical molecular dynamics with appropriate ion-ion pair interaction potentials. The latter ones are obtained by the use of the Starrett and Saumon model providing a consistent treatment of ion correlations in ionized matter so that ion-ion pair interaction potentials and correlation functions are found to be in good agreement with the relevant *ab initio* simulated data in the applicability range of the model [21,22,39]. Molecular-dynamics simulation enables one to characterize temporal evolution of spatial configuration of plasma ions. For every instant configuration, three-dimensional (3D) distribution of total electron density $n_e(\mathbf{r})$ is then reconstructed as a superposition of spherically symmetric electron density distributions $n_e^{\text{PA}}(r)$ of individual pseudoatoms given by the Starrett and Saumon model:

$$n_e(\mathbf{r}) = \sum_{i=1}^{\infty} n_e^{\text{PA}}(|\mathbf{r} - \mathbf{R}_i|), \quad (7)$$

where \mathbf{R}_i is the position vector of the i th nucleus. Each pseudoatom in the Starrett and Saumon model is electrically neutral and contains the central nucleus, bound electrons, and free electrons. The pseudoatom electron density is thus

$$n_e^{\text{PA}}(r) = n_{e,b}(r) + n_e^{\text{scr}}(r), \quad (8)$$

with $n_{e,b}(r)$ and $n_e^{\text{scr}}(r)$ being its bound-electron and free-electron densities, respectively. We note that in the Starrett and Saumon model the former is restricted to the atomic cell of radius r_0 , while the latter is just the density of electrons screening ion-ion Coulomb interaction and therefore entering effective pair interionic potential.

The screening electron density is defined as the difference of free electron densities in the full and external AA systems, respectively:

$$n_e^{\text{scr}}(r) = n_{e,f}^{\text{full}}(r) - n_{e,f}^{\text{ext}}(r). \quad (9)$$

The external system is a system without central nucleus ($Z = 0$) and with the same electron chemical potential μ_e and ion-ion pair correlation function $g(r)$ as in the full AA system. In the Starrett and Saumon model, the function $g(r)$ is generally found through the solution of the Ornstein-Zernike equations [40]. However, to calculate the screening electron density

and the relevant pair interionic potential, it appears accurate enough to represent pair correlation function just in the form of the step function (1) [21,22] and therefore to reduce the full AA system to the neutral Wigner-Seitz sphere (NWS) model [41]. In the present work, we also employ this approach.

In the following, we will focus on the features of the PAMD approach being essential for the current consideration. Specifically, the coupling of the AA model with molecular-dynamics simulations (the expression of the pair interionic potential in terms of the screening electron density and the electron response function) will not be discussed here in detail since in this part our implementation closely follows that one of Starett and Saumon [21].

III. THERMODYNAMIC FUNCTIONS FROM PAMD

Once the electron thermodynamic functions of the full and external AA systems and the 3D electron density (7)

$$k_1^S(\mathbf{r}) = \frac{C}{\beta} \left\{ I_{3/2}(\eta(\mathbf{r})) - \sum_{i=1}^{\infty} [I_{3/2}(\beta[\mu_e - \tilde{V}(|\mathbf{r} - \mathbf{R}_i|)]) - I_{3/2}(\beta[\mu_e - \tilde{V}^{\text{ext}}(|\mathbf{r} - \mathbf{R}_i|)])] \right\}, \quad (12)$$

where $\beta = 1/T$, $C = \sqrt{2}/(\pi^2 \beta^{3/2})$, $I_k(x) = \int_0^{\infty} \frac{y^k dy}{1 + \exp(y-x)}$ is the Fermi-Dirac integral, and the function $\eta(\mathbf{r})$ and effective potentials $\tilde{V}(r)$ and $\tilde{V}^{\text{ext}}(r)$ are found from the relations

$$n_e(\mathbf{r}) = C I_{1/2}(\eta(\mathbf{r})), \quad (13)$$

$$n_e^{\text{full}}(r) = C I_{1/2}(\beta[\mu_e - \tilde{V}(r)]), \quad (14)$$

$$n_e^{\text{ext}}(r) = C I_{1/2}(\beta[\mu_e - \tilde{V}^{\text{ext}}(r)]). \quad (15)$$

If the electron densities $n_e^{\text{full}}(r)$ and $n_e^{\text{ext}}(r)$ were calculated with a semiclassical AA model, then the effective electron potentials $\tilde{V}(r)$ and $\tilde{V}^{\text{ext}}(r)$ would be coincident with their self-consistent counterparts $V(r)$ and $V^{\text{ext}}(r)$.

Explicitly singling out the summed contributions from individual pseudoatoms, one circumvents the need for numerical integration of the 3D function $I_{3/2}(\eta(\mathbf{r}))$, which may strongly diverge at the nuclear positions, getting $\propto \varrho^{-5/2}$ in the semiclassical case, where $\varrho = |\mathbf{r} - \mathbf{R}_i|$. The function (12) is, however, also divergent at the nuclear positions in the semiclassical approximation, though this divergence is not so rapid as for its first term $C I_{3/2}(\eta(\mathbf{r}))/\beta$. Indeed, the electron density (7) close to the i th nucleus may be written as

$$n_e(\varrho) = C I_{1/2}(\eta(\varrho)) \approx C I_{1/2}(\eta_0(\varrho)) + \delta n_{e,i}, \quad (16)$$

where

$$\eta_0(\varrho) = \beta[\mu_e - \tilde{V}(\varrho)] \quad (17)$$

and making use of the fact that $\tilde{V}^{\text{ext}}(\varrho)$ is a bounded function:

$$\begin{aligned} \delta n_{e,i} = & -C I_{1/2}(\beta[\mu_e - \tilde{V}^{\text{ext}}(\varrho = 0)]) \\ & + \sum_{j \neq i}^{\infty} n_e^{\text{PA}}(|\mathbf{R}_j - \mathbf{R}_i|). \end{aligned} \quad (18)$$

for a set of plasma-ion configurations have been calculated, thermodynamic functions for the relevant configurations are obtained and the averaging over those is then performed. In calculating additive contributions to the Helmholtz free energy (i.e., kinetic energy, exchange-correlation energy, and entropy), it was proposed [32] to explicitly single out the summed contributions from individual pseudoatoms found by using the full and external AA systems. Specifically, for the kinetic energy K attributed to a computational volume V with N nuclei one gets:

$$K = N K^{\text{PA}} + K_1^S. \quad (10)$$

Here the part of kinetic energy K_1^S containing no contributions from individual pseudoatoms K^{PA} is evaluated in the semiclassical approximation:

$$K_1^S = \int_V k_1^S(\mathbf{r}) d\mathbf{r}, \quad (11)$$

Then, taking into account the properties of the Fermi-Dirac integrals (see Ref. [42]),

$$I'_k(x) = k I_{k-1}(x) \quad (k > 0), \quad (19)$$

$$I_k(x) = \frac{x^{k+1}}{k+1} + O(x^k) \text{ at } x \gg 1,$$

one therefore obtains that

$$\eta(\varrho) \approx \eta_0(\varrho) + \frac{\delta n_{e,i}}{C \sqrt{\eta_0(\varrho)}}, \quad (20)$$

$$\begin{aligned} I_{3/2}(\eta(\varrho)) & \approx I_{3/2}(\eta_0(\varrho)) + \delta n_{e,i} \eta_0(\varrho)/C \\ & \approx I_{3/2}(\eta_0(\varrho)) - \delta n_{e,i} \beta \tilde{V}(\varrho)/C, \end{aligned} \quad (21)$$

$$k_1^S(\varrho) \approx -\delta n_{e,i} \tilde{V}(\varrho). \quad (22)$$

In the semiclassical case, the function (22) diverges as $1/\varrho$. The divergence would be more weak if one employed semiclassical approximation only for the high-energy AA electron orbitals or just calculated all the wave functions by solving the relativistic Dirac equation. Even though the function (22) is not divergent (e.g., if all the wave functions are found from the nonrelativistic Schrödinger equation), it may peak sharply at the nuclear positions, thus making numerical integration rather complicated when the number of nuclei in the computational volume is large enough. We therefore propose, in a like manner as above, to explicitly single out the summed contributions from the functions (22), the integration of which becomes one-dimensional due to the spherical symmetry of those:

$$\begin{aligned} K_1^S = & - \left(\sum_{i=1}^N \delta n_{e,i} \right) 4\pi \int_0^{\infty} \tilde{V}(\varrho) f_{\text{cut}}(\varrho) \varrho^2 d\varrho \\ & + \int_V k^S(\mathbf{r}) d\mathbf{r}, \end{aligned} \quad (23)$$

$$k^S(\mathbf{r}) = k_1^S(\mathbf{r}) + \sum_{i=1}^{\infty} \delta n_{e,i} \tilde{V}(|\mathbf{r} - \mathbf{R}_i|) f_{\text{cut}}(|\mathbf{r} - \mathbf{R}_i|), \quad (24)$$

where the function $f_{\text{cut}}(\varrho) = e^{-\varrho/r_0}$ is introduced to ensure a rapid convergence of the radial integral. The function (24) is free of singularities (even in the semiclassical case) and hence can be integrated on a rather coarse grid. Similar techniques may also be employed to improve the methods of calculating exchange-correlation energy and electron entropy.

In the present implementation of the PAMD approach the pressure is obtained from the relativistic virial theorem (see, e.g., Ref. [41]):

$$3PV = 3NT + 2B + E_{\text{el}} + C_{\text{xc}}, \quad (25)$$

where E_{el} is the energy of electrostatic interactions evaluated by using a method of Ref. [32] and C_{xc} is the exchange-correlation contribution. In the present work we take no account of the electron correlation energy and disregard the explicit temperature dependence of the exchange energy. In this approximation C_{xc} becomes simply the Kohn-Sham exchange energy [43]. The term B in Eq. (25) is calculated by implementing the same decomposition as in Eq. (10):

$$B = NB^{\text{PA}} + B_1^S = N(B^{\text{full}} - B^{\text{ext}}) + B_1^S. \quad (26)$$

Here, the terms B^{full} and B^{ext} represent average values of the operator $\hat{B} = \frac{1}{2}(\hat{K} + \hat{B}_1)$ in the full and external AA systems, respectively, where \hat{K} is the relativistic kinetic-energy operator, $\hat{B}_1 = 2c^2 \begin{pmatrix} 0 & \\ & I \end{pmatrix}$ (c is the speed of light, I is the 2×2 unity matrix). The term B_1^S as well as the similar contribution to the kinetic energy K_1^S is calculated in the semiclassical approximation, thus yielding $B_1^S = K_1^S$.

IV. APPROXIMATIONS FOR THE MEAN ION CHARGE AND THE FREE ELECTRON DENSITY

The ion thermal contributions to the AA thermodynamic functions depend on the values of the mean ion charge Z_0 [see Eqs. (2) and (6)]—a nonobservable quantity that may be defined in various ways [44,45]. Specifically, in the context of the Liberman model [15], one may define the mean ion charge as [45]

(i) the ratio of the electron density at the boundary of the atomic cell to the average ion density:

$$Z_0 = Z_{\text{WS}} = n_e(r_0)/n_i; \quad (27)$$

(ii) the number of continuum electrons within the atomic cell:

$$Z_0 = Z_* = \int_0^{\infty} w(\varepsilon) n(\varepsilon) d\varepsilon = Z - \sum_{nlj} (2j+1) n(\varepsilon_{nlj}) \cdot \int_0^{\infty} [P_{nlj}^2(r) + Q_{nlj}^2(r)] \theta(r_0 - r) dr, \quad (28)$$

where

$$w(\varepsilon) = \sum_{lj} (2j+1) \int_0^{r_0} [P_{\varepsilon lj}^2(r) + Q_{\varepsilon lj}^2(r)] dr, \quad (29)$$

$$n(\varepsilon) = \{1 + \exp[\beta(\varepsilon - \mu_e)]\}^{-1}, \quad (30)$$

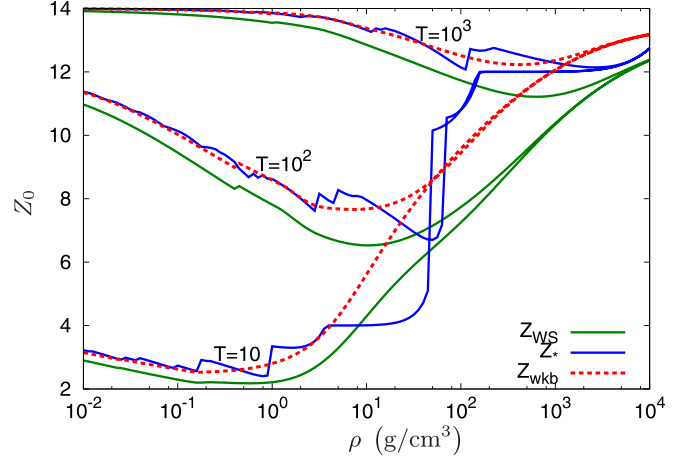


FIG. 1. Isotherms of the silicon mean ion charge at temperatures $T = 10, 10^2$, and 10^3 eV calculated by using various approximations in the context of the Liberman model.

with $P(r)/r$ and $Q(r)/r$ being the major and the minor radial components of the relativistic wave function, respectively, attributed to a bound (continuum) electron state characterized by its principal quantum number n (free-electron energy ε), orbital, l , and total, j , angular momenta;

(iii) a semiclassical formula differing from Eq. (28) by the use of semiclassical expression for the density of states:

$$Z_0 = Z_{\text{wkb}} = \int_0^{\infty} w_{\text{wkb}}(\varepsilon) n(\varepsilon) d\varepsilon, \quad (31)$$

$$w_{\text{wkb}}(\varepsilon) = \frac{4\sqrt{2}}{\pi} \int_0^{r_0} \sqrt{\varepsilon - V(r)} r^2 dr.$$

Figure 1 presents isotherms of the silicon mean ion charge at various temperatures calculated by Eqs. (27), (28), and (31). The definition (27) takes no account of the nonuniformity of free-electron density and therefore systematically underestimates the mean ion charge—it may be shown that at $\Gamma \ll Z_0$ this underestimation approximately amounts to 0.3Γ . Though the definition (28) allows for the free-electron-density nonuniformity, it gives rise to nonphysical jumps as the bound-electron states disappear under the pressure ionization, whereas all the observables exhibit no jumps due to counterbalancing effect of shape resonances simultaneously emerging in the continuum-electron density of states [46]. The definition (31) is free from the drawbacks of the previous ones: On average, the values (31) are close to those ones given by Eq. (28) with the jumps smoothed.

In the NWS model, one can calculate the mean ion charge by using just the same Eqs. (27), (28), and (31) as in the Liberman model. The only minor feature is encountered here in calculating Z_* : Following Ref. [21], the Heaviside function $\theta(r_0 - r)$ in Eq. (28) is replaced by the approximating smooth function $f_c(r) = (1 + e^{-1/0.05})/[1 + e^{-(r-r_0)/(0.05r_0)}]$ —in fact, the effect of the substitution $\theta(r_0 - r) \rightarrow f_c(r)$ on the mean ion charge is generally insignificant.

PAMD-simulated data are also sensitive to the choice of the screening electron density (9), governing the interionic

potential, and therefore to the mean ion charge in the pseudoatom picture. The latter one can be expressed in terms of the screening electron density as

$$Z_0 = 4\pi \int_0^\infty n_e^{\text{scr}}(r) r^2 dr = 4\pi \int_0^\infty [n_{e,f}^{\text{full}}(r) - n_{e,f}^{\text{ext}}(r)] r^2 dr. \quad (32)$$

$$4\pi r^2 n_{e,f}^{\text{full}}(r) = \int_0^\infty d\varepsilon n(\varepsilon) \sum_{lj} (2j+1) [P_{elj}^2(r) + Q_{elj}^2(r)] + [1 - f_c(r)] \sum_{nlj} (2j+1) n(\varepsilon_{nlj}) [P_{nlj}^2(r) + Q_{nlj}^2(r)], \quad (33)$$

$$4\pi r^2 n_{e,f}^{\text{ext}}(r) = \int_0^\infty d\varepsilon n(\varepsilon) \sum_{lj} (2j+1) [(P_{elj}^{\text{ext}}(r))^2 + (Q_{elj}^{\text{ext}}(r))^2]. \quad (34)$$

The second definition is similar to that one given by Eq. (31) and obtained by substituting into Eq. (32) free-electron densities in the full,

$$n_{e,f}^{\text{full}}(r) = \frac{\sqrt{2}}{\pi^2} \int_0^\infty d\varepsilon n(\varepsilon) \sqrt{\varepsilon - V(r)}, \quad (35)$$

and external,

$$n_{e,f}^{\text{ext}}(r) = \frac{\sqrt{2}}{\pi^2} \int_0^\infty d\varepsilon n(\varepsilon) \sqrt{\varepsilon - V^{\text{ext}}(r)}, \quad (36)$$

AA systems. The relevant pseudoatom mean ion charge is also denoted as Z_{wkb} since the disagreement of its values with those ones defined with Eq. (31) is generally insignificant. This definition of the mean ion charge is also used for the NWS model when accounting for ion correlations in the OCP and CHS approximations.

It should be emphasized that the mean ion charge (31) and free-electron densities (35) and (36) are actually not the same as their counterparts in the semiclassical (orbital-free) AA/PAMD approach (see Fig. 2), being the functions of the electron chemical potential and self-consistent electron potential obtained from the AA model with quantum-mechanical description of electrons. This enables one not only to avoid nonphysical jumps under the pressure ionization but also to allow for the atomic-shell oscillations under the temperature ionization, unfeasible with the pure semiclassical approach.

It should be noted that the sensitivity of the PAMD-simulated thermodynamic functions to the discontinuities in the temperature and material-density dependences of the free-electron density $n_{e,f}^{\text{full}}(r)$ is not as crucial as that one observed for the ion contributions to the EOS evaluated in the OCP and (especially) CHS approximations with respect to the jumps of the mean ion charge Z_* . The reason is that those discontinuities affect the PAMD results only in the indirect way—through the dependence of interionic potential on the screening electron density (9). This is also well illustrated by the relevant PAMD-simulated pressure isochores of aluminum and silicon of Ref. [32] with no visible discontinuities imprinted. However, in a broader density range than that one addressed in Ref. [32] the effect of the discontinuities discussed on the PAMD results may become more pronounced—especially if one examines ion contributions to the internal energy and pressure just from the PAMD simulations rather than the total PAMD thermodynamic functions.

In PAMD simulations, two definitions of the pseudoatom mean ion charge were employed. The first one is similar to the definition (28) with $\theta(r_0 - r)$ replaced by $f_c(r)$ and therefore is just the same as Z_* in the NWS model. This definition corresponds to the following expressions for the free-electron densities in the full and external AA systems in Eq. (32):

On the other hand, possible discontinuities of the PAMD results may be smoothed by using *ad hoc* weighting factors $M(\varepsilon_{nlj})$ in the bound-electron density—bound-state survival probabilities in the electron-ion scattering process [21]:

$$M(\varepsilon_{nlj}) = \text{erf}(-2\sqrt{\ln 2} \varepsilon_{nlj}/\gamma), \quad (37)$$

where $\text{erf}(x)$ is the error function and γ is the electron-ion collision frequency. We do not, however, use such smoothing because, in our opinion, it does not properly represent the physics of the pressure ionization. In particular, it works only when a bound state is about to be pressure ionized and does not allow for the fact that a continuum resonance is actually a quasibound state [46]. The semiclassical formulas (35) and (36) provide an alternative smoothing which, unlike (37), works well long before and after a bound state is pressure ionized (see Fig. 1). Such a broad semiclassical smoothing seems to be reasonable for calculation of thermodynamic functions, though it does not necessarily improve the description of structural properties. In particular, it gives no way to

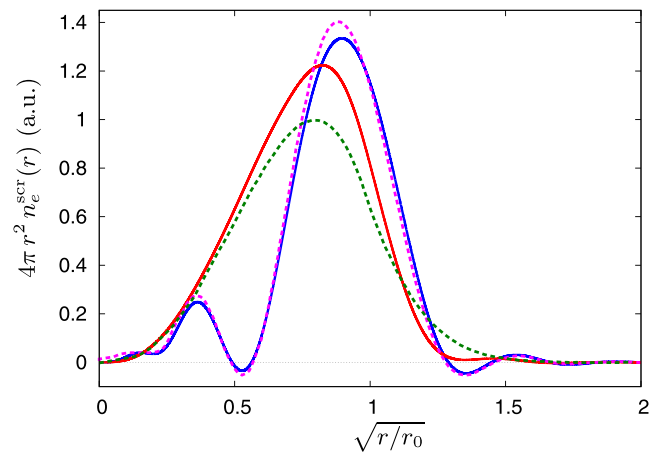


FIG. 2. Present-work radial screening electron density for aluminum at $\rho = 2.7 \text{ g/cm}^3$, $T = 2 \text{ eV}$ calculated with quantum-mechanical description of electrons and various definitions of free-electron densities—(33) and (34) (blue solid curve) and (35) and (36) (red solid curve)—as compared to the calculations of Ref. [21] with free-electron densities (33) and (34) (magenta dashed curve) and their semiclassical counterparts similar to (35) and (36) (green dashed curve).

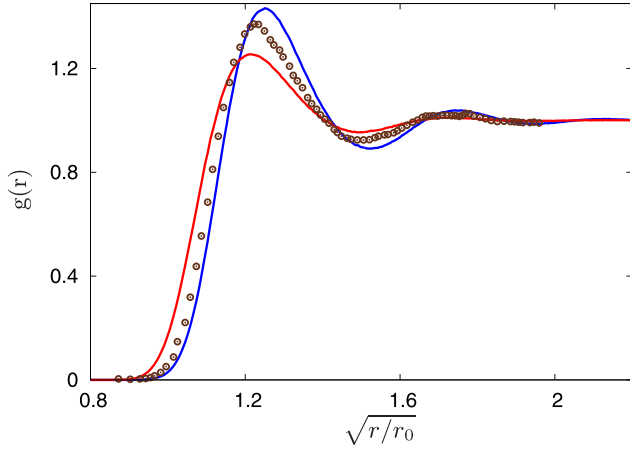


FIG. 3. Ion-ion pair distribution functions for aluminum at $\rho = 2.7 \text{ g/cm}^3$, $T = 2 \text{ eV}$, calculated with PAMD using various definitions of the screening electron density providing the pseudoatom mean ion charge $Z_0 = Z_*$ (blue curve) and $Z_0 = Z_{\text{wkb}}$ (red curve), as compared to QMD simulations of Ref. [21] (brown circles).

represent the features in the screening electron density due to quantum effects such as the wave-function orthogonality [32] (see Fig. 2). Besides that, the values of Z_* may provide more physically sound estimation of the number of free electrons per atom at certain temperature-density points as compared to those ones of Z_{wkb} . Specifically, this may happen in the absence of well-occupied weakly bound electron states or continuum resonances. As a result, in some situations PAMD simulations utilizing the definition of screening electron density specific to $Z_0 = Z_*$ provide better agreement of the ion-ion pair distribution functions with the *ab initio* simulation data than those ones performed with the alternative definition yielding $Z_0 = Z_{\text{wkb}}$ (Fig. 3). For all the reasons above, the distinctions of the relevant PAMD-simulated data (see Figs. 5–9 and 22) may be considered as a measure of uncertainty of the present-work PAMD implementation.

V. THE EOS OF SILICON

In present paper, molecular-dynamics simulations and the NWS or Liberman’s AA-model calculations were performed with the Moloch [47] and RESEOS [48–50] codes, respectively. The Moloch simulations were performed in the canonical NVT ensemble. The ion temperature was controlled by the Langevin thermostat. The time step varied between 0.03 and 0.3 fs depending on temperature and density. The number of particles ($\approx 40\,000$) and time steps (20 000–30 000) in our molecular-dynamics simulations were comparable to those ones employed in Ref. [32]. The accuracy of the Moloch simulations was tested by comparing the calculated ion-ion pair distribution functions for aluminum to the similar results of Starrett and Saumon [51]. As one can see from Fig. 4, the pair distribution functions from the two implementations of the PAMD approach are in excellent agreement thus corroborating the Moloch simulations.

For the Moloch simulations, the RESEOS code provides the NWS-model electron densities and pair interionic potentials being very similar to those ones calculated by Starrett and

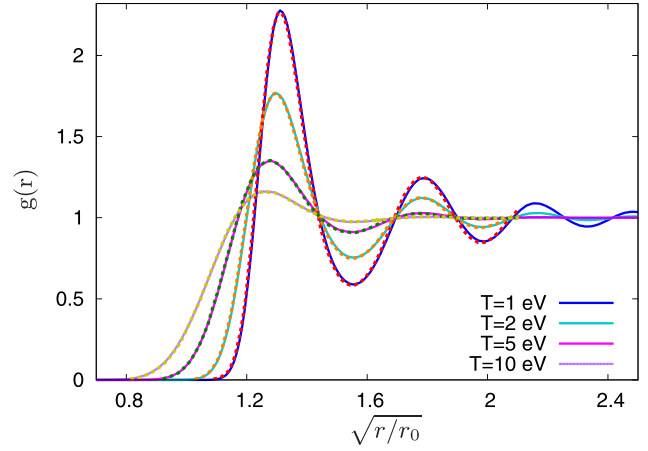


FIG. 4. Ion-ion pair distribution functions for aluminum at a density $\rho = 6.3 \text{ g/cm}^3$ and various temperatures obtained with PAMD utilizing the definition of the screening electron density providing the pseudoatom mean ion charge $Z_0 = Z_*$. Solid and dashed curves corresponding to the simulations of the present work and of Ref. [51], respectively, coincide almost perfectly.

Saumon assuming the same definitions of the free-electron density and the mean ion charge (see Figs. 2 and 4). At the same time, thermodynamic functions of the present work may

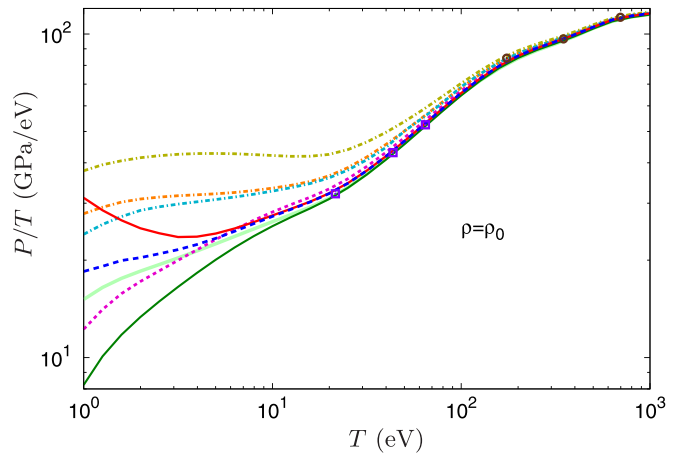


FIG. 5. Isochores of the pressure-to-temperature ratio for normal density silicon ($\rho = \rho_0 = 2.329 \text{ g/cm}^3$) calculated by using the PAMD approach and AA models with various approximations for the ion thermal contribution to the EOS as compared to the *ab initio* simulation data of Ref. [7]. Red solid and blue dashed curves correspond to the PAMD calculations utilizing the screening electron density definitions providing the pseudoatom mean ion charge $Z_0 = Z_{\text{wkb}}$ and $Z_0 = Z_*$, respectively; dark green and light green solid curves correspond respectively to the NWS and Liberman AA-model calculations with the ideal-gas approximation for the ion thermal contribution; magenta dashed curve—to the NWS calculation with the OCP approximation for the ion thermal contribution utilizing $Z_0 = Z_{\text{wkb}}$; orange dashed-dotted, cyan dash-dotted, and yellow dash-dotted curves—to the NWS calculations with the CHS approximation for the ion thermal contribution utilizing $Z_0 = Z_{\text{wkb}}$, $Z_0 = Z_*$, and $Z_0 = Z_{\text{WS}}$, respectively. Squares and circles represent the QMD and PIMC simulation data [7], respectively.

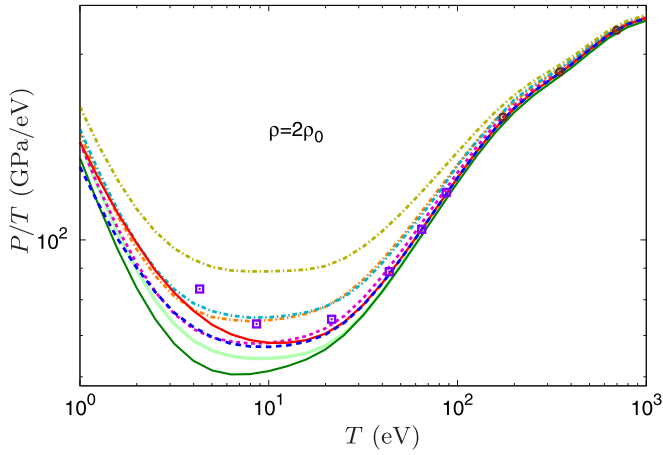


FIG. 6. Isochores of the pressure-to-temperature ratio for silicon at $\rho = 2\rho_0$. The colors, lines, and symbols have the same meanings as in Fig. 5.

differ from the relevant calculated data of Starrett and Saumon (see Fig. 23 and the related discussion).

In Figs. 5–9 the isochores of the pressure-to-temperature ratio for silicon at densities $\rho = \rho_0 \dots 7\rho_0$ (ρ_0 is the normal density) calculated by using the PAMD approach and the AA models above with various approximations for ion thermal contribution to the EOS including the ideal-gas approximation,

$$E_{[1/\text{atom}]} = E_e + 1.5T, \quad P = P_e + T n_i, \quad (38)$$

are compared to the relevant QMD and PIMC *ab initio* simulation data [7].

Unlike Liberman’s model, the NWS model accounts for the electron-density nonuniformity beyond the atomic cell. However, to provide a more realistic description, a similarly consistent treatment should also be done for external ions. Since both the Liberman and NWS models employ a crude approximation (1) for the pair correlation function, there is generally no reason to believe that the NWS model does offer more accurate results. Thus, distinctions between the calcu-

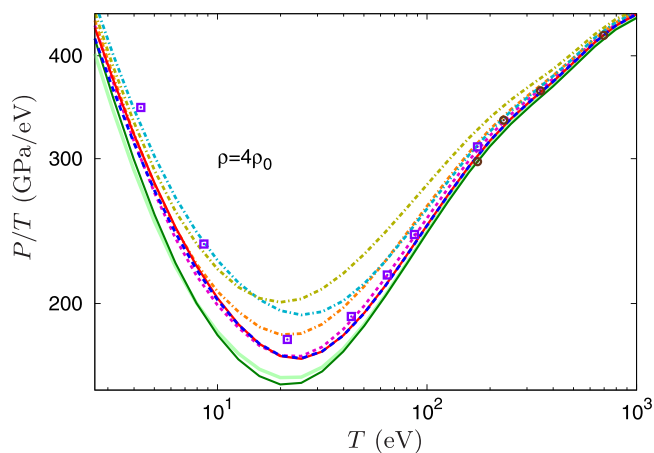


FIG. 7. Isochores of the pressure-to-temperature ratio for silicon at $\rho = 4\rho_0$. The colors, lines, and symbols have the same meanings as in Fig. 5.

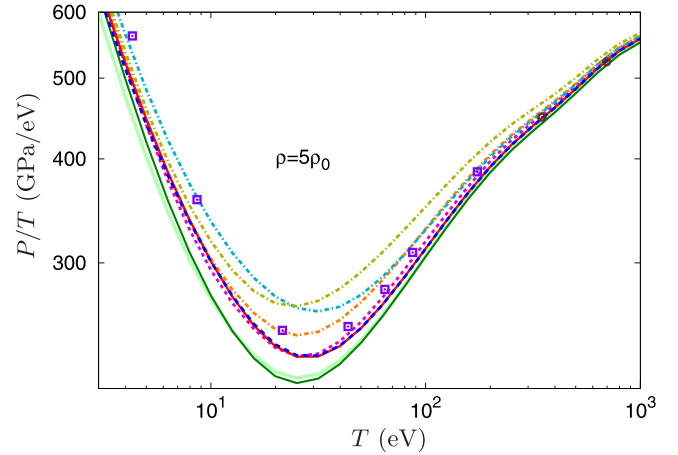


FIG. 8. Isochores of the pressure-to-temperature ratio for silicon at $\rho = 5\rho_0$. The colors, lines, and symbols have the same meanings as in Fig. 5.

lated data obtained with the two models (being important for silicon at $\rho \lesssim 2\rho_0$ and $T \lesssim 10$ eV only; see Figs. 5–9) may be recognized as a measure of uncertainty in the electron thermodynamic quantities specific to the average-atom-in-jellium models [8,10] with the electrically neutral atomic cell. Such an uncertainty is therefore inherited by the PAMD approach as it employs the NWS-model calculated data.

It should be noted that the uncertainty of electron thermodynamic functions discussed stems not only from the distinction of the Liberman and NWS models themselves but also from different methods employed to calculate the electron pressure. In the NWS model, the latter was evaluated using the virial theorem (25), while in the Liberman model—the numerical differentiation of the Helmholtz free energy preexpressed in terms of entropy [18] (see Appendix A for a discussion of various methods to calculate pressure in AA models).

The results of the PAMD calculations presented in Figs. 5–9 were obtained by using two definitions of the screening electron density providing the pseudoatom mean

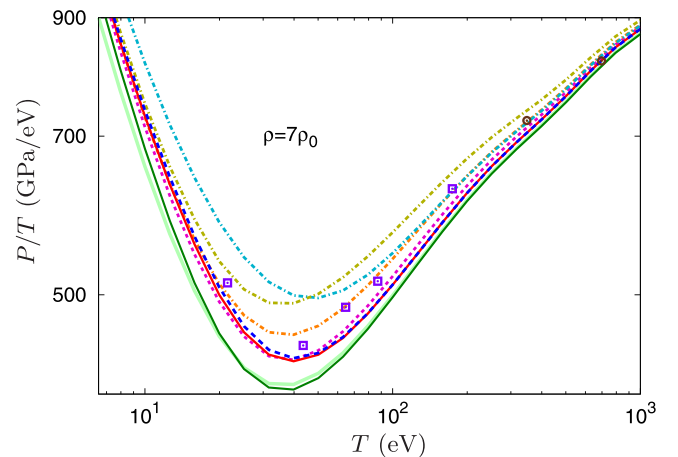


FIG. 9. Isochores of the pressure-to-temperature ratio for silicon at $\rho = 7\rho_0$. The colors, lines, and symbols have the same meanings as in Fig. 5.

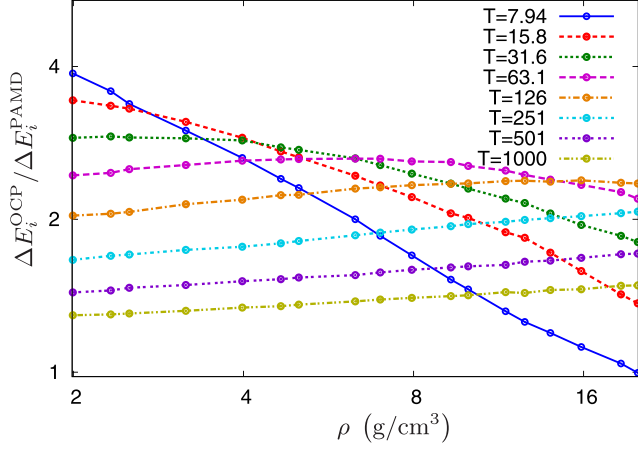


FIG. 10. Ratios of the OCP corrections to the NWS-model internal energy ΔE_i^{OCP} evaluated at various temperatures T (eV) of silicon and $Z_0 = Z_{\text{wkb}}$ to their PAMD counterparts ΔE_i^{PAMD} found with the screening electron density definition providing $Z_0 = Z_{\text{wkb}}$.

ion charge $Z_0 = Z_{\text{wkb}}$ and $Z_0 = Z_*$. One can see that the distinctions of the relevant PAMD-calculated data, that may be considered as a measure of uncertainty of the present-work implementation of the PAMD approach, are evidently more pronounced at low temperatures ($T \lesssim 10$ eV).

Description of the effects due to ion correlations with PAMD calculations or under the OCP approximation improves the agreement with *ab initio* simulations as compared to the use of the ideal-gas approximation [52]. The employment of the CHS approximation traditionally suggests the evaluation of the mean ion charge according to Eq. (27) [9,20,25] which underestimates mean ion charge due to disregard of the free-electron-density nonuniformity. This leads to the overestimation of ion-core radius r_* (6) and therefore to the overestimation of the total pressure as clearly observed in Figs. 5–9. The use of alternative definitions of $Z_0 = Z_{\text{wkb}}$ or $Z_0 = Z_*$ generally allows one to eliminate this overestimation to a large extent.

Various approximations to model ion thermal contribution to the AA-based equations of state may evidently be tested by making comparisons with more accurate calculations. For example, in Ref. [53] the results of *ab initio* QMD and PIMC simulations [6] were employed to examine Cowan’s ion-thermal model [26] as well as to calibrate a semiempirical model demonstrating much more rapid decay of heat capacity with increasing temperature than the Cowan model. Here we employ the PAMD simulations to validate much simpler OCP and CHS representations of the ion thermal contribution to the AA-based EOS [54]. To do this, we consider the ratios of the ion-correlation corrections to the AA internal energy (ΔE_i) and pressure (ΔP_i) evaluated under the OCP and CHS approximations to their counterparts obtained with the PAMD simulations (see Figs. 10–14). The corrections were found by subtracting the NWS-model energy and pressure with the ions treated in the ideal-gas approximation (38) from the relevant total values allowing for ion correlations. In Figs. 15–18 we also compare the ratios $\Delta P_i / \Delta E_i$ governing the difference in the EOS stiffness. One can see from the figures that in some temperature and material density domains the OCP and CHS

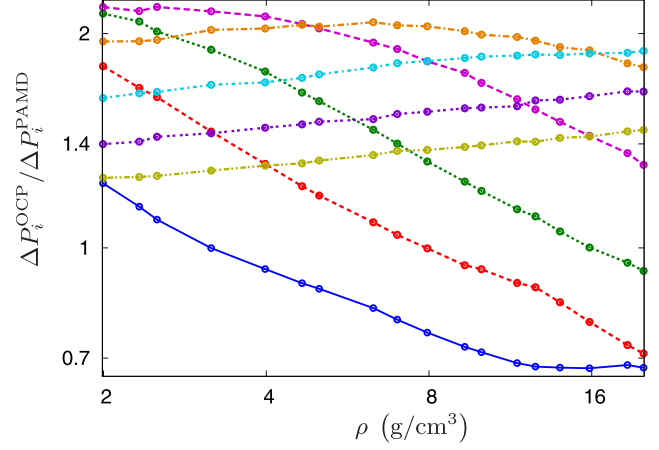


FIG. 11. Ratios of the OCP corrections to the NWS-model pressure ΔP_i^{OCP} evaluated at various temperatures of silicon and $Z_0 = Z_{\text{wkb}}$ to their PAMD counterparts ΔP_i^{PAMD} found with the screening electron density definition providing $Z_0 = Z_{\text{wkb}}$. The colors and lines have the same meanings as in Fig. 10.

approximations may overestimate or, conversely, underestimate the corrections ΔE_i and ΔP_i as well as their ratio by several times relative to their PAMD counterparts. At the same time, in the temperature range considered, the difference of the corrections ΔP_i and ΔE_i obtained from the PAMD calculations utilizing the screening electron density definitions providing $Z_0 = Z_*$ (not shown in figures) and $Z_0 = Z_{\text{wkb}}$ does not exceed 30%.

As evident from the figures, the OCP approximation provides relatively accurate corrections ΔP_i at $T \sim 10$ eV but overestimates those markedly with increasing temperature. The correction ΔE_i in the OCP approximation is overestimated almost everywhere, especially when $T \simeq 10$ –60 eV and $\rho \sim \rho_0$. As a result, the OCP ratio $\Delta P_i / \Delta E_i$ is strongly underestimated at $T \sim 10$ eV, thus leading to some underestimation of the shock Hugoniot stiffness [see Fig. 20(a)]. At

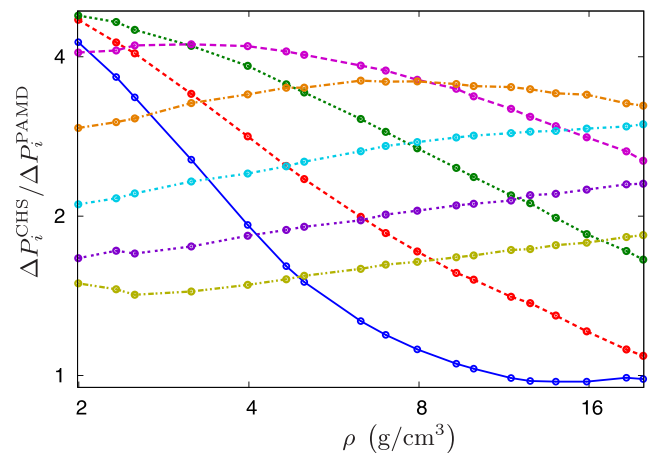


FIG. 12. Ratios of the CHS corrections to the NWS-model pressure ΔP_i^{CHS} evaluated at various temperatures of silicon and $Z_0 = Z_{\text{wkb}}$ to their PAMD counterparts ΔP_i^{PAMD} found with the screening electron density definition providing $Z_0 = Z_{\text{wkb}}$. The colors and lines have the same meanings as in Fig. 10.

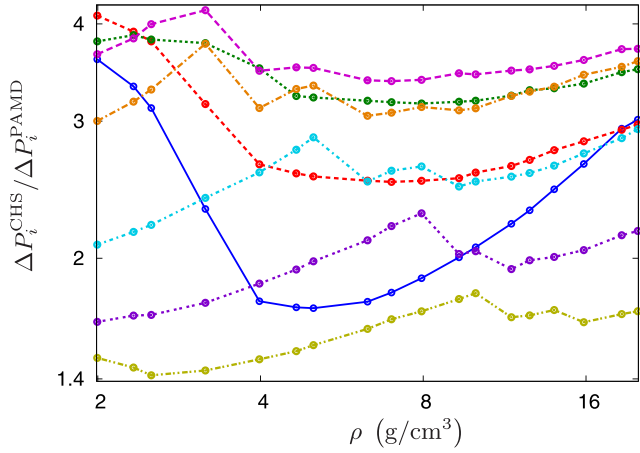


FIG. 13. Ratios of the CHS corrections to the NWS-model pressure ΔP_i^{CHS} evaluated at various temperatures of silicon and $Z_0 = Z_*$ to their PAMD counterparts ΔP_i^{PAMD} found with the screening electron density definition providing $Z_0 = Z_{\text{wkb}}$. The colors and lines have the same meanings as in Fig. 10.

high temperatures ($T \gtrsim 200$ eV) the OCP corrections ΔE_i and ΔP_i are both overestimated, but their ratio appears to be very close to that one given by the PAMD calculations.

In comparing the PAMD and OCP ion-correlation corrections, it should be remembered that the OCP model provides only the correction to the plasma electrostatic energy, while the PAMD correction to the internal energy also includes the corrections to the electron kinetic and exchange energies. As one can see from Fig. 19, the correction to the electrostatic energy dominates at high temperatures ($T \gtrsim 100$ eV). At lower temperatures ($T \lesssim 10$ eV) the ion-correlation corrections to the electron kinetic and exchange energies become non-negligible—the fact, which is not represented by the simplified OCP model. At the same time, the OCP corrections appear to be closer to the total PAMD ones than to the partial PAMD corrections to the electrostatic energy (the latter may

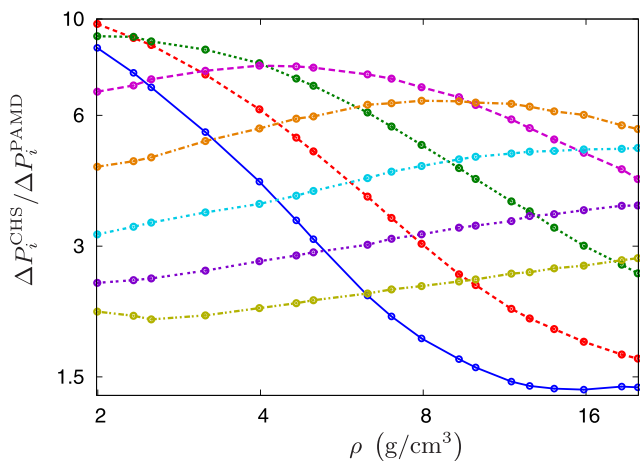


FIG. 14. Ratios of the CHS corrections to the NWS-model pressure ΔP_i^{CHS} evaluated at various temperatures of silicon and $Z_0 = Z_{\text{WS}}$ to their PAMD counterparts ΔP_i^{PAMD} found with the screening electron density definition providing $Z_0 = Z_{\text{wkb}}$. The colors and lines have the same meanings as in Fig. 10.

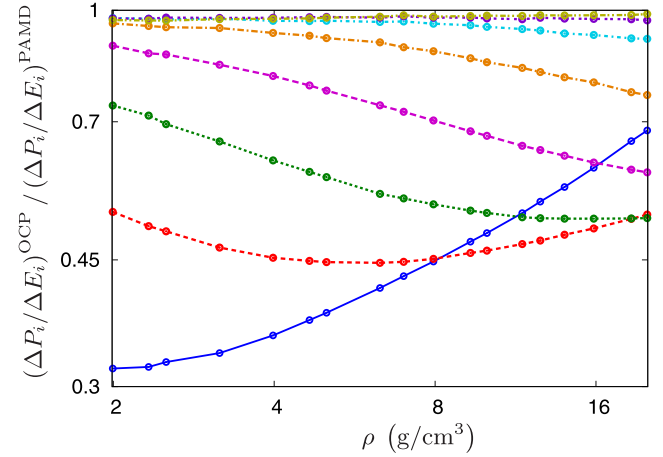


FIG. 15. The OCP pressure-to-internal energy-corrections ratios $(\Delta P_i / \Delta E_i)^{\text{OCP}}$ evaluated using the NWS model at various temperatures of silicon and $Z_0 = Z_{\text{wkb}}$ as divided by their PAMD counterparts $(\Delta P_i / \Delta E_i)^{\text{PAMD}}$ found with the screening electron density definition providing $Z_0 = Z_{\text{wkb}}$. The colors and lines have the same meanings as in Fig. 10.

even be negative at low temperatures while the OCP and the total PAMD corrections are always positive).

As mentioned above, the use of the CHS approximation with $Z_0 = Z_{\text{WS}}$ strongly overestimates the correction ΔP_i (up to an order of magnitude) and therefore leads to the excessive stiffness of the shock Hugoniot [Fig. 20(a)]. In the temperature range considered, the CHS ΔP_i evaluated with $Z_0 = Z_{\text{wkb}}$ and $Z_0 = Z_*$ generally appear to be overestimated as well, though such an overestimation is less pronounced than that one at $Z_0 = Z_{\text{WS}}$ and, in the context of the EOS stiffness, is largely counterbalanced by the simultaneous overestimation of the correction ΔE_i (being the same in both the CHS and OCP approximations). Here, we also note that the definition

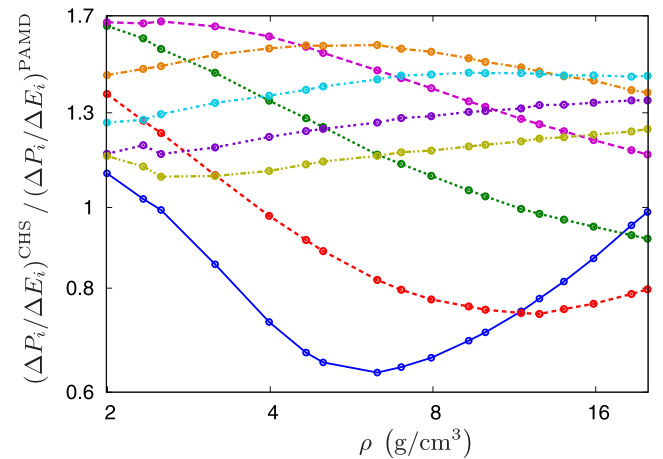


FIG. 16. The CHS pressure-to-internal energy-corrections ratios $(\Delta P_i / \Delta E_i)^{\text{CHS}}$ evaluated using the NWS model at various temperatures of silicon and $Z_0 = Z_{\text{wkb}}$ as divided by their PAMD counterparts $(\Delta P_i / \Delta E_i)^{\text{PAMD}}$ found with the screening electron density definition providing $Z_0 = Z_{\text{wkb}}$. The colors and lines have the same meanings as in Fig. 10.

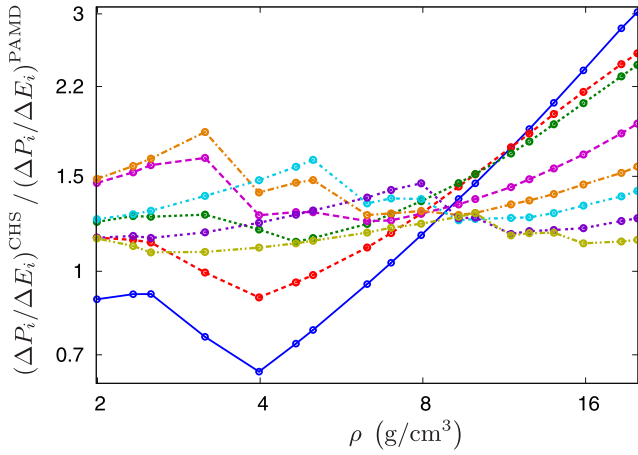


FIG. 17. The CHS pressure-to-internal energy-corrections ratios $(\Delta P_i/\Delta E_i)^{\text{CHS}}$ evaluated using the NWS model at various temperatures of silicon and $Z_0 = Z_*$ as divided by their PAMD counterparts $(\Delta P_i/\Delta E_i)^{\text{PAMD}}$ found with the screening electron density definition providing $Z_0 = Z_{\text{wkb}}$. The colors and lines have the same meanings as in Fig. 10.

$Z_0 = Z_{\text{wkb}}$, unlike $Z_0 = Z_*$, provides smooth dependence of the correction ΔP_i on temperature and material density.

Similarly, the PAMD approach may also be employed to validate other promising approximations for the ion-correlation corrections discussed, as the latter ones do appear.

Figure 20 presents the calculated principal shock Hugoniot of silicon in both the ρ - P and T - P/T variables. As one can see from Fig. 20(a), in the ρ - P frame the PAMD-calculated shock Hugoniot appears to be in the closest agreement with those ones obtained using the AA models with the ideal-gas ion thermal contribution to the EOS. The reason is that the pressure and internal energy changes due to ion correlations, being responsible for higher stiffness (ΔP_i) and softness (ΔE_i) of the shock Hugoniot, in fact counterbalance

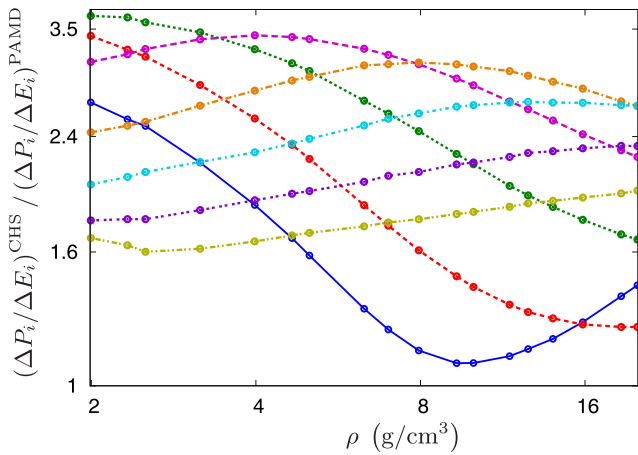


FIG. 18. The CHS pressure-to-internal energy-corrections ratios $(\Delta P_i/\Delta E_i)^{\text{CHS}}$ evaluated using the NWS model at various temperatures of silicon and $Z_0 = Z_{\text{WS}}$ as divided by their PAMD counterparts $(\Delta P_i/\Delta E_i)^{\text{PAMD}}$ found with the screening electron density definition providing $Z_0 = Z_{\text{wkb}}$. The colors and lines have the same meanings as in Fig. 10.

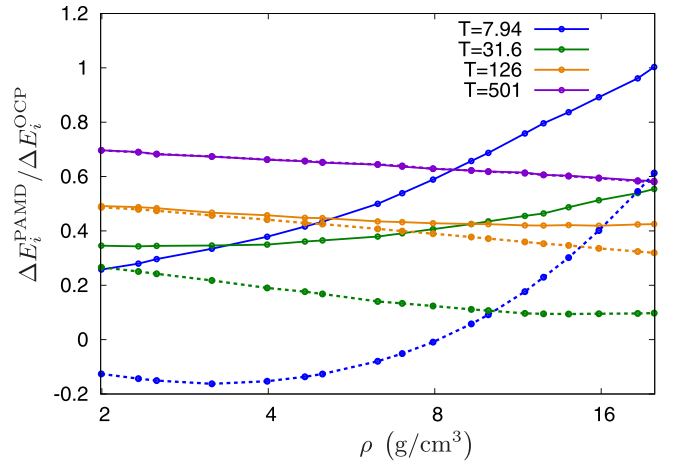


FIG. 19. Ratios of the PAMD corrections to the NWS-model internal energy ΔE_i^{PAMD} found at various temperatures of silicon with the screening electron density definition providing $Z_0 = Z_{\text{wkb}}$ to their OCP counterparts ΔE_i^{OCP} evaluated with $Z_0 = Z_{\text{wkb}}$. Solid curves correspond to the total PAMD corrections and dashed curves—to corrections to the electrostatic energy only (violet solid and dashed curves almost coincide with each other).

each other. This, however, is not the case for the shock Hugoniot in the T - P/T frame [see Fig. 20(b)], thus illustrating the fact that temperature measurements at the shock front may serve as an important supplementary tool for the experimental verification of the EOS data.

In Fig. 21 the PAMD and NWS-model principal shock Hugoniot of silicon are compared to the relevant theoretical data obtained from *ab initio* [7] and the original PAMD [32] simulations. One can see that the shock Hugoniot are in a satisfactory overall agreement, with the PAMD curves somewhat overestimating the maximum compression as compared to that one resulting from the *ab initio* simulations. This distinction may arise from inability of taking account of the finite-ion-size effects in evaluating the PAMD interionic potentials as well as from the inaccuracy of the QMD simulations at maximum-compression temperatures ($T \sim 100$ eV) being extremely high to handle by the QMD method. The latter inaccuracy is typically manifested as the underestimation of the QMD-calculated internal energy at $T \approx 100$ eV by a few percentages as illustrated by Fig. 22.

In this connection we note that the maximum compression along the shock Hugoniot may be estimated by the approximate analytical formula of Ref. [55]. For silicon, the maximum compression ratio $\sigma_{\text{max}} = \rho_{\text{max}}/\rho_0$ predicted by this formula ($\sigma_{\text{max}} = 5.13$) is in a good agreement with the results of both the *ab initio* simulations of Ref. [7] and PAMD calculations— $\sigma_{\text{max}} = 4.99$ and 5.23, respectively.

Figure 21 also shows that the present-work PAMD curve agrees well with the result of the original PAMD simulations [32] at $P \gtrsim 2 \times 10^3$ GPa ($T \gtrsim 15$ eV)—the fact that one cannot, however, observe at lower pressures. To analyze possible reasons of this disagreement we consider the pressure along the normal-density isochore of aluminum (the nearby atomic-number element) calculated by using the PAMD approach and the NWS AA model with the ideal-gas approximation for

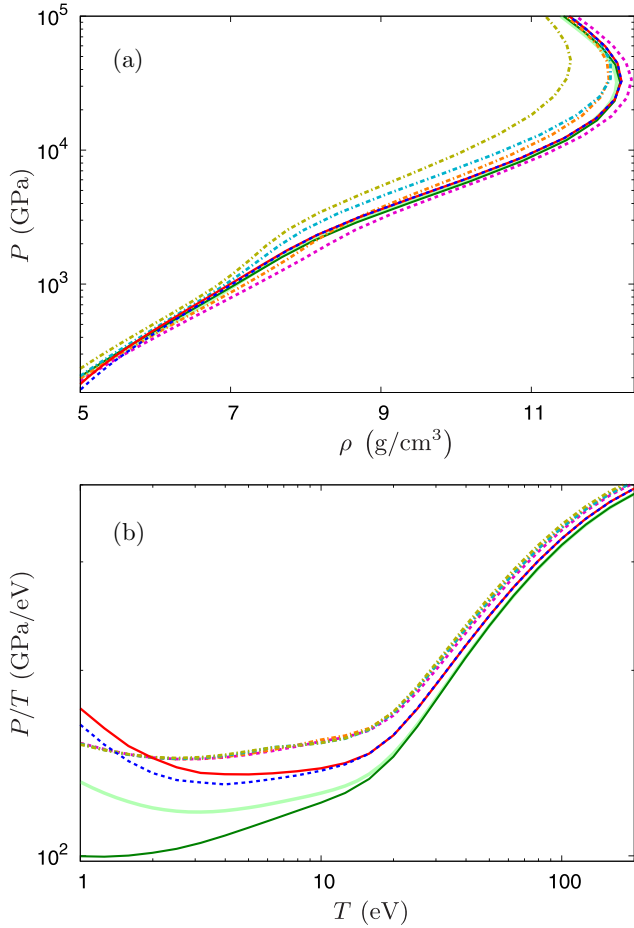


FIG. 20. Principal shock Hugoniots of silicon calculated by using the PAMD approach and AA models with various approximations for the ion thermal contribution to the EOS. Red solid and blue dashed curves correspond to the PAMD calculations with the screening electron density definitions providing $Z_0 = Z_{wkb}$ and $Z_0 = Z_*$, respectively; dark green and light green solid curves correspond respectively to the NWS and Liberman AA-model calculations with the ideal-gas approximation for the ion thermal contribution; magenta dashed curve—to the NWS calculation with the OCP approximation for the ion thermal contribution utilizing $Z_0 = Z_{wkb}$; orange dashed-dotted, cyan dash-dotted, and yellow dash-dotted curves—to the NWS calculations with the CHS approximation for the ion thermal contribution utilizing $Z_0 = Z_{wkb}$, $Z_0 = Z_*$, and $Z_0 = Z_{WS}$, respectively. In Fig. 20(b), magenta dashed, orange dashed-dotted, cyan dash-dotted, and yellow dash-dotted curves almost coincide with each other.

plasma ions. As one can see from Fig. 23, calculated data of the present work and of Ref. [32] are in close agreement at $T \simeq 10\text{--}15$ eV, while at lower temperatures the calculations of Ref. [32] provide higher pressures, especially those ones done with the NWS model.

In this connection, we note that a reason for higher NWS-model pressure at lower temperatures in Ref. [32] is also responsible for the rise in the relevant PAMD-calculated pressure. Indeed, any inaccuracies of the NWS-model energy and associated pressure are directly inherited by their PAMD counterparts [e.g., through the terms $N K^{PA}$, $N B^{PA}$ in

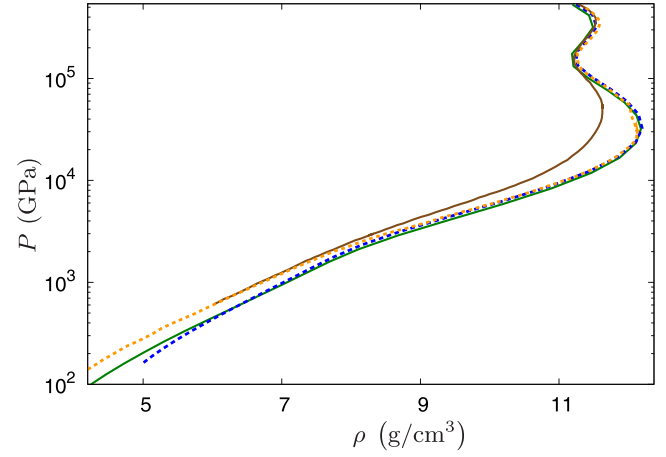


FIG. 21. Principal shock Hugoniots of silicon calculated by using the NWS AA model with the ideal-gas approximation for the ion thermal contribution (dark green solid curve) and the PAMD approach with the screening electron density definition providing $Z_0 = Z_*$ (blue dashed curve) as compared to the similar PAMD calculations ($Z_0 = Z_*$) of Ref. [32] (orange dashed curve) and *ab initio* (QMD + PIMC) simulations of Ref. [7] (brown solid curve).

Eqs. (10) and (26)]. This fact implied a need to examine the calculation of pressure with the NWS model in a more detail.

As it is known, there is a number of formulas to calculate pressure in the context of AA models [46] (see Appendix A). In particular, in the NWS model electron pressure given by

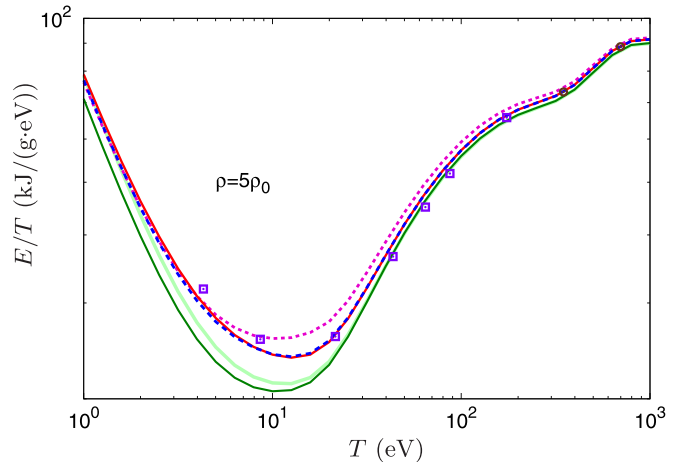


FIG. 22. Isochores of the internal energy-to-temperature ratio for silicon at $\rho = 5\rho_0 = 11.645$ g/cm³ calculated by using the PAMD approach and AA models with various approximations for the ion thermal contribution to the EOS as compared to the *ab initio* simulation data of Ref. [3]. Red solid and blue dashed curves correspond to the PAMD calculations with the screening electron density definitions providing $Z_0 = Z_{wkb}$ and $Z_0 = Z_*$, respectively; dark green and light green solid curves correspond respectively to the NWS and Liberman AA-model calculations with the ideal-gas approximation for the ion thermal contribution; magenta dashed curve—to the NWS calculation with the OCP approximation for the ion thermal contribution utilizing $Z_0 = Z_{wkb}$. Squares and circles represent the QMD and PIMC simulation data [3], respectively.

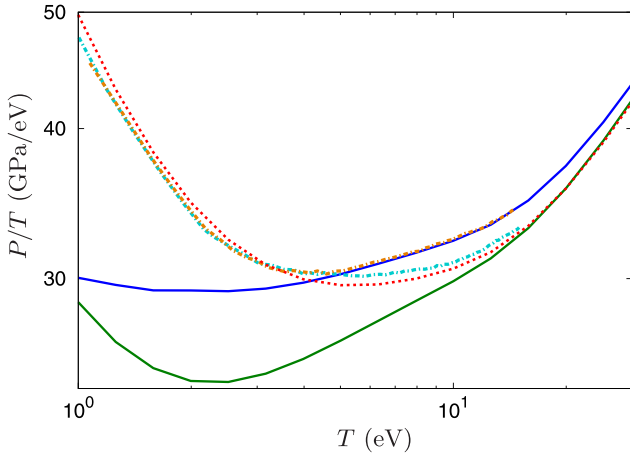


FIG. 23. Isochores of the pressure-to-temperature ratio for normal density aluminum ($\rho = \rho_0 = 2.7 \text{ g/cm}^3$) as calculated by using the NWS model with the ideal-gas approximation for plasma ions (present work—green solid curve, Ref. [32]—cyan dashed-dotted curve) and the PAMD approach with the screening electron density definition providing $Z_0 = Z_*$ (present work—blue solid curve, Ref. [32]—orange dashed-dotted curve). Red dashed curve corresponds to the present-work NWS-model calculation with the ideal-gas approximation for plasma ions and the term ΔP (40) of Eq. (39) omitted.

the virial theorem may be written as [41]

$$P_e = P_e^0 + \Delta P, \quad (39)$$

where P_e^0 reproduces the Thomas-Fermi-Dirac pressure [11] to within the relativistic corrections and

$$\Delta P = \frac{n_e^0}{r_0^3} \int_{r_0}^{\infty} r^3 \frac{dV_{\text{el}}(r)}{dr} dr \quad (40)$$

with $n_e^0 = \lim_{r \rightarrow \infty} n_e(r)$ and $V_{\text{el}}(r)$ being the electrostatic potential created by all the charges.

Comparisons of pressures found in the present work directly from the virial theorem (25) (yielding relatively small pressure obtained as the difference of large values) and those ones given by Eq. (39) (free of such a difference) show that the relevant discrepancies are less than 0.3%. This numerical test safely suggests that the present-work results are correct and therefore enables one to make a conclusion that the pressure calculated in Ref. [32] is overestimated at $T \lesssim 10 \text{ eV}$.

As one can see from Fig. 23, the inclusion of the term ΔP is of crucial importance at low temperatures near the normal density—without this term the pressure (39) would be far from that one calculated directly by Eq. (25). At the same time, our calculations closely reproduce the results of Ref. [32] when the term ΔP of Eq. (39) is omitted. However, we cannot definitely conclude that this coincidence is not fortuitous and the missing term ΔP was actually the reason of the overestimation of pressure in Ref. [32]. The main conclusion is that the silicon pressure of Ref. [32] could be overestimated at $T \lesssim 10 \text{ eV}$ similar to the aluminum pressure thus leading to a stiffer shock Hugoniot of Ref. [32] at low temperatures as compared to our calculations (Fig. 21). One more conclusion is that the relative effect of ion correlations on the calculated pressure obtained in Ref. [32] seems to be underestimated, at

least at low temperatures near the normal density: The calculations of Ref. [32] shown in Fig. 23 predict very small effect of ion correlations at $T \lesssim 10 \text{ eV}$ —much smaller than, e.g., the OCP model does. In contrast, our calculations show that the OCP model is not as poor as may be inferred from the results of Ref. [32]: It provides at least the correct order-of-magnitude evaluation of the ion pressure and generally improves the agreement of the AA-based pressure with the PAMD one at $T \sim 10 \text{ eV}$.

VI. THE EOS OF SILICON DIOXIDE

To construct the EOS of silicon dioxide (SiO_2), one also needs to generate the EOS of oxygen. In doing this, we have restricted our consideration to the PAMD calculations with the screening electron density definition providing $Z_0 = Z_{\text{wkb}}$. Ion-correlation corrections to the internal energy and pressure of oxygen obtained by using the OCP and CHS approximations and the PAMD approach follow the same trends as those ones revealed for silicon.

In the present work, the EOS of silicon dioxide was constructed from the silicon and oxygen EOS by using the linear mixing rule [9,26,56–59]. Specifically, we have employed the so-called excess-pressure mixing rule [56,57,59] implying the equality of excess pressures (i.e., pressures with the ideal-gas ion contribution excluded) of pure components at their respective partial densities ρ_k , which satisfy the additivity condition for partial volumes $1/\rho_k$. Such mixing rule can be derived from the variational principle [9,58] with its accuracy being high enough in the WDM regime [56,57,59]: The difference of pressures obtained by the direct molecular-dynamics simulations of mixtures and from the excess-pressure mixing rule is generally of the order of 1% or less. So, the use of the mixing rule is justified because its own accuracy is better than the accuracy of the underlying physical models for pure elements addressed in the present work.

The theoretical and experimental shock Hugoniots are compared in Fig. 24. One can see that taking account of ion correlations in the OCP approximation softens the NWS-model shock Hugoniot and worsens the agreement with the experimental data [60–62] and *ab initio* QMD simulations [63] as compared to the ideal-gas approximation. The reasons for this may be twofold. First, the comparison to the PAMD simulations above shows that the OCP approximation overestimates the correction to the internal energy ΔE_i likely due to the fact that overidealized OCP system provides poor quantitative estimation of the Coulomb interaction effects in real strongly coupled plasmas. Specifically, the polarization of the electron gas under the attraction of nuclei, being essential in real plasmas, is disregarded in the OCP approximation. The overestimation of the correction ΔE_i , in turn, results in the underestimation of the EOS stiffness. Second, even if the correction ΔE_i were not overestimated in the OCP approximation, the relevant ratio $\Delta P_i^{\text{OCP}}/(\rho \Delta E_i^{\text{OCP}})$ is equal to $\frac{1}{3}$ [see Eqs. (3) and (4)] [64] being smaller than the typical values of the ratio

$$G_r = P_{\text{th}}/(\rho E_{\text{th}}), \quad (41)$$

where P_{th} and E_{th} are the thermal components of pressure and internal energy. For this reason, the use of the OCP

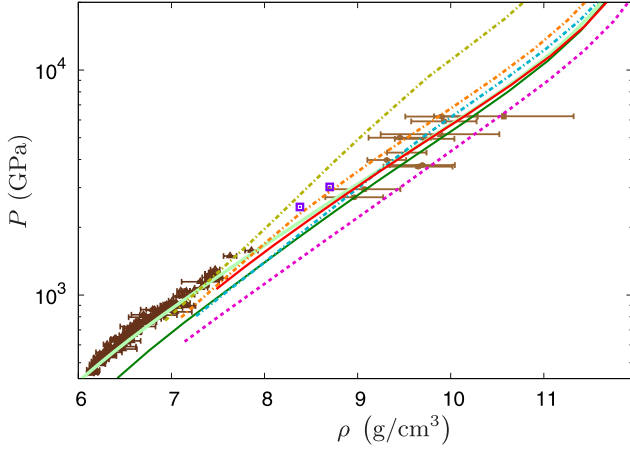


FIG. 24. Principal shock Hugoniot of SiO_2 calculated by using the PAMD approach and AA models with various approximations for the ion thermal contribution to the EOS. Red solid curve corresponds to the PAMD calculation with the screening electron density definition providing $Z_0 = Z_{\text{wkb}}$; dark green and light green solid curves correspond respectively to the NWS and Liberman AA-model calculations with the ideal-gas approximation for the ion thermal contribution; magenta dashed curve—to the NWS calculation with the OCP approximation for the ion thermal contribution utilizing $Z_0 = Z_{\text{wkb}}$; orange dashed-dotted, cyan dash-dotted, and yellow dash-dotted curves—to the NWS calculations with the CHS approximation for the ion thermal contribution utilizing $Z_0 = Z_{\text{wkb}}$, $Z_0 = Z_*$, and $Z_0 = Z_{\text{WS}}$, respectively. Dark and light brown symbols represent the Z-machine [60,61] and NIF [62] experimental data, respectively, and violet squares—the QMD simulations of Ref. [63].

approximation results in the lowering of the ratio (41) and, consequently, in softening of the shock Hugoniot.

To avoid such underestimation of the ratio (41), one needs to account for the finite-ion-size effects. Doing this by means of the additional hard-sphere-model correction to pressure $T n_i \delta P_i^{\text{HS}}(\eta)$ with $Z_0 = Z_{\text{wkb}}$ or $Z_0 = Z_*$ enhances the stiffness of the shock Hugoniot as compared to the OCP approximation, thus providing the better agreement with the experimental data and QMD simulations. One should, however, note that the comparisons to the PAMD simulations above reveal an overestimation of the net correction ΔP_i in this case being partially counterbalanced by the overestimation of the correction ΔE_i . The CHS approximation with $Z_0 = Z_{\text{WS}}$ further enhances the correction ΔP_i , thus yielding well pronounced overestimation of the shock Hugoniot stiffness as compared to the experimental data obtained at the NIF facility [62]. This therefore suggests that common practice of using the mean-ion-charge definition $Z_0 = Z_{\text{WS}}$ in the CHS model is unjustified.

While the NWS and Liberman AA-model shock Hugoniot of silicon are in the closest agreement in ρ - P frame (see Fig. 20), for silicon dioxide one can observe pronounced distinctions between the similar ones at $P < 100$ Mbar—the NWS model yields a softer shock Hugoniot. Unlike the NWS-model shock Hugoniot (with the ideal-gas approximation for the ion thermal contribution), the similar Liberman-model shock Hugoniot agrees reasonably well with the Z-machine measurements at $P \lesssim 15$ Mbar [60,61]. To identify the source

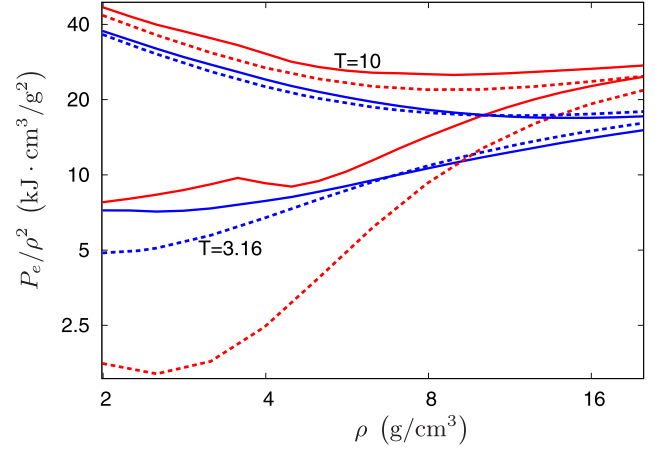


FIG. 25. Electron pressure for silicon (blue curves) and oxygen (red curves) at $T = 3.16$ and 10 eV calculated with the Liberman (solid curves) and NWS (dashed curves) models.

of these distinctions, in Fig. 25 we compare electron pressure for silicon and oxygen at $T = 3.16$ and 10 eV calculated with the NWS and Liberman models. One can see that relative differences of the electron pressure calculated with these models are much larger for oxygen than for silicon. For this reason, distinctions between the NWS and Liberman AA-model shock Hugoniot for silicon dioxide get more pronounced.

A drastic disagreement of the oxygen electron pressures from the Liberman and NWS models observed in Fig. 25 at the lowest temperature considered ($T \approx 3$ eV) and densities $\rho \lesssim 4$ g/cm³ is due to the fact that self-consistent Coulomb potential in the NWS model does not yet vanish at the boundary of the atomic cell due to the presence of the weakly bound $2p$ -shell electrons, the wave functions of which extend beyond the atomic cell. At the same time, in the Liberman model this potential beyond the atomic cell is identically zero by definition. In such situations electron pressures obtained from the Liberman and NWS models would be different, even when those are found with the same method, and the use of different methods to calculate electron pressure (i.e., the virial theorem for the NWS model and the differentiation of the Helmholtz free energy for the Liberman model) generally enhances this disagreement. At low temperatures the $2p$ shell is pressure ionized at $\rho \approx 4$ g/cm³ after that the electron pressures for oxygen obtained from the Liberman and NWS models become much closer together (see Fig. 25). For silicon, one can also observe a noticeable disagreement of the relevant electron pressures being, however, less pronounced than for oxygen and occurring at somewhat lower densities, at which weakly bound $3p$ -shell electrons or the corresponding sharp continuum resonance exist (the $3p$ shell is pressure ionized at $\rho \approx 1$ g/cm³).

It should be noted that single-center AA models cannot properly describe weakly bound states with wave functions extending beyond the atomic cell. In fact, such states are strongly disturbed by the plasma environment and their energy levels are smeared out into broad structures similar to energy bands in solid state [65,66]. In the NWS model, the electron thermodynamic functions contain contributions from the space region beyond the atomic cell. It is also unlikely that

these contributions are correctly represented by the single-center approach, especially when the simplified step-function (1) treatment of interionic correlations is employed. In the Liberman model, the thermodynamic functions are evaluated solely inside the atomic cell, even when the bound-state wave functions have long tails beyond the cell. Though this approach may be recognized as more simplified with respect to the NWS model, in some cases its use may show better results. But, even so, one cannot perceive such results as more justified than those ones given by the NWS model.

The underestimation of electron pressure by the NWS model immediately affects the PAMD results as the latter ones directly include thermodynamic functions obtained with the NWS model [see, e.g., the terms NK^{PA} , NB^{PA} in Eqs. (10) and (26)]. Due to this underestimation the pressure along the PAMD shock Hugoniot is also underestimated as compared to the QMD simulations, though the account of the ion correlations with PAMD leads to some increase of the relevant shock-Hugoniot pressure in relation to that one given by the NWS-model utilizing the ideal-gas approximation for plasma ions. Alongside this, the PAMD principal shock Hugoniot of silicon dioxide at higher pressures, $P \simeq 30\text{--}60$ Mbar, agrees well with the NIF experimental data of Ref. [62].

As one can see from the calculations presented, the PAMD approach provides most reliable results at fairly high temperatures ($T \gtrsim 10$ eV). In this connection, it should be noted that all these calculations were done with no regard for the explicit temperature dependence of the electron exchange potential. However, with the Liberman model the latter was generally found to have no significant effect on the total thermodynamic functions at $T \gtrsim 10$ eV, even when this dependence was treated by using a simple semiclassical approximation [67–70] overestimating the effect. Therefore, the use of the zero-temperature exchange potential [43] does not affect general conclusions on the validity of the PAMD calculations of the present work and on the accuracy of the OCP and CHS approximations for the ion thermal contribution to the EOS.

VII. CONCLUSION

Modifications to the original formulation of the PAMD approach [32] are proposed. The modifications include an improved method to calculate thermodynamic functions in the context of the PAMD simulations and an alternative technique to evaluate the screening electron density and the corresponding mean ion charge. The latter provides another option to avoid nonphysical jumps under the pressure ionization as compared to the *ad hoc* smoothing through the use of the bound-state survival probabilities in the electron-ion scattering process [weighting factors in the bound-electron density (37)] that was proposed earlier in Ref. [21]. With these modifications implemented on the base of the RESEOS average atom and Moloch molecular dynamics codes, the silicon and oxygen equations of state were generated and then employed to construct the equation of state of silicon dioxide by using the linear mixing rule.

The PAMD-calculated principal shock Hugoniots of silicon are found to be in a satisfactory overall agreement with the relevant theoretical data obtained from the QMD and PIMC

ab initio [7] simulations, with the PAMD curves somewhat overestimating the maximum compression. The latter may arise from inability of taking account of the finite-ion-size effects in evaluating the PAMD interionic potentials as well as from the inaccuracy of the QMD simulations at maximum-compression temperatures ($T \sim 100$ eV), being extremely high for the QMD method.

For silicon dioxide the PAMD principal shock Hugoniot agrees well with recent high-pressure ($P \simeq 30\text{--}60$ Mbar) experimental data obtained at the NIF facility [62]. At lower pressures the PAMD shock Hugoniot appears to be less accurate due to the well pronounced underestimation of the NWS-model electron pressure in oxygen (unlike silicon) immediately affecting the PAMD results as the latter ones directly include the thermodynamic functions from the NWS model. This underestimation is illustrated by the comparison to the relevant Liberman-model calculated data and may be recognized as a measure of uncertainty of the EOS electron component specific to the atom-in-jellium models with the electrically neutral atomic cell.

The effect of the ion correlations on the PAMD-calculated shock Hugoniots of silicon and silicon dioxide in the ρ - P frame appears to be small since the relevant pressure and internal energy changes, being responsible, respectively, for stiffening and softening of the shock Hugoniot, in fact counterbalance each other.

The PAMD approach allows one to eliminate uncertainties connected with the ion thermal contribution to thermodynamic functions being specific to the average-atom-based equations of state. Comparisons to the PAMD simulations provide an immediate possibility to examine various approximations to model ion thermal contribution to those EOS since the consistent treatment of ion correlations is the main advantage of the PAMD approach over the AA models. For silicon we have tested the OCP and CHS approximations against the PAMD simulations using various methods to specify mean ion charge. We have shown that the ion-correlation corrections to pressure ΔP_i and internal energy ΔE_i obtained with PAMD may differ by several times from those ones obtained under the OCP and CHS approximations. The correction ΔE_i in the OCP and CHS approximations and the correction ΔP_i in the CHS approximation are usually overestimated at $T \gtrsim 10$ eV as compared to their PAMD counterparts. However, the inaccuracies of the OCP and CHS corrections $\Delta P_i(\rho, T)$ and $\Delta E_i(\rho, T)$ can partially counterbalance each other in their ratio which is responsible for the EOS stiffness. The use of the mean-ion-charge definition $Z_0 = Z_{\text{WS}}$, commonly adopted for the CHS approximation, generally yields underestimated values of Z_0 with the resulting significant overestimation of the ion pressure and should be therefore considered as unjustified. At the same time, our results for the ion-correlation correction to pressure differ from those ones obtained earlier in Ref. [32] where this correction seems to be underestimated at low temperatures ($T \lesssim 10$ eV) and densities near the normal density. The similar examination against the PAMD data may also be performed to validate other promising and more sophisticated approximations for the ion-correlation corrections, as they appear, and thereby to further extend the range of applicability of computationally inexpensive average-atom-based equations of state.

APPENDIX A: ON THE EVALUATION OF ELECTRON PRESSURE IN THE AVERAGE-ATOM MODELS

In the AA models electron pressure may be evaluated by at least three alternative approaches [46]: by the differentiation of the specific Helmholtz free energy with respect to material density:

$$P_e(\rho, T) = \rho^2 \frac{\partial F_e(\rho, T)}{\partial \rho}, \quad (\text{A1})$$

by using the virial theorem, and calculating the momentum flux density (i.e., via the stress tensor). In a completely consistent model, rigorously derived through the variational minimization of the thermodynamic potential, all three approaches yield the same result. To the best of our knowledge, only three types of the AA models meet this condition: the semiclassical Thomas-Fermi model [71] along with its improved versions, the VAAQP model [41,72], and the Hartree-Fock-Slater model with quasiperiodic boundary conditions [9,20,25,67,73]. The Liberman and NWS AA models addressed in the present paper do not rigorously satisfy the variational principle thus leading to differing values of pressure calculated by alternative methods.

The nonrelativistic virial theorem is usually formulated as follows [cf. Eq. (25)]:

$$3P_e V = 2K + E_{\text{el}} + C_{\text{xc}}. \quad (\text{A2})$$

This formulation is, however, not necessarily correct with respect to a part of some larger system (e.g., to the atomic cell in an atom-in-jellium model). On the other hand, in the context of a spherically symmetrical model one can define the pressure as the diagonal component P_{rr} of the stress tensor (which includes a local-density exchange-correlation correction) at the boundary of the spherical volume V . If this volume is neutral (what is specific to the atomic cell in the Liberman, NWS, and Hartree-Fock-Slater models), then the pressure P_{rr} satisfies the following form of the virial theorem [46]:

$$3P_{rr} V = 3P_e V = K + \tilde{K} + E_{\text{el}} + C_{\text{xc}}, \quad (\text{A3})$$

where the quantity

$$\tilde{K} = \frac{1}{2} \sum_{\nu} n(\varepsilon_{\nu}) \int_V |\nabla \psi_{\nu}(\mathbf{r})|^2 d\mathbf{r}, \quad (\text{A4})$$

in general, differs from the kinetic energy

$$K = -\frac{1}{2} \sum_{\nu} n(\varepsilon_{\nu}) \int_V \psi_{\nu}^*(\mathbf{r}) \nabla^2 \psi_{\nu}(\mathbf{r}) d\mathbf{r} \quad (\text{A5})$$

(the values of K and \tilde{K} coincide in the special case of quasiperiodic boundary conditions that may be imposed in the Hartree-Fock-Slater model [9,20,25,67,73]). The subscript ν in Eqs. (A4) and (A5) runs over all nonrelativistic single-electron states characterized by the orbital, magnetic, and spin projection quantum numbers l , m_l , and m_s , respectively, and bound-state principal quantum numbers n or continuum-state energies ε .

The relativistic virial theorem may be formulated in terms of the surface integral over the boundary of the atomic cell

(see Ref. [15]):

$$P_e = -\frac{ic}{8\pi r_0^3} \sum_{\nu} n(\varepsilon_{\nu}) \oint_{r=r_0} [\psi_{\nu}^+(\mathbf{r}) \mathbf{a}(\mathbf{r} \cdot \nabla) \psi_{\nu}(\mathbf{r}) + \text{c.c.}] d\mathbf{S} + P_{\text{xc}}(n_e(r_0), T), \quad (\text{A6})$$

where $a_k = \begin{pmatrix} 0 & \sigma_k \\ \sigma_k & 0 \end{pmatrix}$ (σ_k are the Pauli matrices),

$$P_{\text{xc}}(n_e, T) = -f_{\text{xc}}(n_e, T) + n_e V_{\text{xc}}(n_e, T) \quad (\text{A7})$$

with f_{xc} being the exchange-correlation free-energy density related to the exchange-correlation potential by

$$V_{\text{xc}}(n_e, T) = \frac{\partial f_{\text{xc}}(n_e, T)}{\partial n_e}. \quad (\text{A8})$$

The summation over ν in Eq. (A6) runs over all relativistic single-electron states.

Starting from Eq. (A6), the following expression for pressure was derived in Ref. [74]:

$$P_e = \frac{c}{4\pi r_0^2} \sum_{\nu} n(\varepsilon_{\nu}) (Q_{\nu}(r_0) P'_{\nu}(r_0) - P_{\nu}(r_0) Q'_{\nu}(r_0)) + P_{\text{xc}}(n_e(r_0), T). \quad (\text{A9})$$

This expression may also be obtained directly from Eq. (25) if one takes into account the following relation stemming from the Dirac equation:

$$[\varepsilon_{\nu} - V(r) - r V'(r)] [P_{\nu}^2(r) + Q_{\nu}^2(r)] = \frac{d}{dr} (r [Q_{\nu}(r) P'_{\nu}(r) - P_{\nu}(r) Q'_{\nu}(r)]). \quad (\text{A10})$$

Regarding Eq. (A9) it should be noted that just the same expression was obtained later in Ref. [23] in the context of the relativistic Liberman model by using the definition of pressure as the P_{rr} component of the stress tensor. In the nonrelativistic limit Eq. (A9) reduces to (A3) [23,74]. Thus, in the context of the AA models the relativistic virial theorem is consistent both with the definition of pressure in terms of the stress tensor and with the nonrelativistic virial theorem expressed by Eq. (A3). At the same time, the relativistic virial theorem does not generally correspond to a more conventional form (A2) of the nonrelativistic virial theorem. This fact is essential for the Liberman model since two forms of the virial theorem represented by Eqs. (A2) and (A3) may lead to pronounced distinctions between the relevant pressures found with this model. This is illustrated by the results of Ref. [74] in which the pressure was calculated in the context of the Liberman model using both Eq. (A9) and the following formula:

$$P_e = \frac{c}{4\pi r_0^2} \sum_{\nu} n(\varepsilon_{\nu}) [Q_{\nu}(r_0) P'_{\nu}(r_0) - P_{\nu}(r_0) \cdot Q'_{\nu}(r_0) - \frac{1}{r_0} P_{\nu}(r_0) Q_{\nu}(r_0)] + P_{\text{xc}}(n_e(r_0), T). \quad (\text{A11})$$

This formula as well as Eq. (A9) may be derived by making an approximate differentiation of the Helmholtz free energy [74] but unlike Eq. (A9) it recovers a more conventional form (A2) of the virial theorem in the nonrelativistic limit. In Ref. [74] it was, however, obtained that in contrast to Eq. (A9) the formula (A11) does not provide finite values of the normal material density (the pressure never takes negative values even

at zero temperature). At the same time, the values of pressure calculated by Eqs. (A9) and (A11) generally become closer with increasing temperature or density. So, in the context of the Liberman model the evaluation of pressure with Eqs. (A3) or (A9) is, in general, more justified as compared to the use of Eqs. (A2) or (A11).

One more formula for electron pressure (both for the non-relativistic and relativistic cases) was proposed in Ref. [75] by considering the average of all diagonal components of the stress tensor instead of the P_{rr} component only:

$$P_e = \frac{1}{3}(P_{rr} + P_{\theta\theta} + P_{\varphi\varphi}), \quad (\text{A12})$$

with θ and φ being the angular variables. It is important that at the temperatures high enough, when the semiclassical approximation for free electrons is valid, all the pressure formulas above provide very close results.

In contrast to the Liberman model, the calculation of pressure by the virial theorem in the NWS model is not restricted to the atomic cell. The contribution of electrons beyond the atomic cell is also accounted via the cluster expansion. As a result, the NWS-model pressure formula (39) differs from (A9) in two ways. First, it contains the additional term (40). Second, the pressure is expressed in terms of free-electron wave functions corresponding to the zero potential rather than the average-atom wave functions as in Eq. (A9). The summation over single-electron states is then performed analytically thus yielding the term P_e^0 in Eq. (39). This term formally coincides both with the pressure in the Thomas-Fermi-Dirac model [11] (to within the relativistic corrections) and with the

diagonal components P_{rr} , $P_{\theta\theta}$, and $P_{\varphi\varphi}$ of the stress tensor in the uniform electron gas. Besides that, in the context of the nonrelativistic NWS model the two forms of the virial theorem [the cluster-expansion counterparts of Eqs. (A2) and (A3)] yield the same pressure. However, the NWS model, as well as the Liberman model, is thermodynamically inconsistent in the sense that all the formulas above result in the pressure values being generally different from those ones obtained using Eq. (A1).

Numerical differentiation of the Helmholtz free energy via Eq. (A1) places more stringent requirements on the computational accuracy than the use of the virial theorem or the stress tensor. The sensitivity to numerical inaccuracies is largely reduced if the free energy is precalculated by the numerical integration of electron entropy [18,66]:

$$F_e(\rho, T) = - \int_0^T S_e(\rho, T') dT'. \quad (\text{A13})$$

But this approach is well suited only for the Liberman model since the presence of long-range Friedel oscillations of the electron density in the NWS model renders the calculations at near-zero temperatures rather difficult. Therefore, the use of the virial theorem provides the most practical way to calculate pressure in the context of the NWS model and the PAMD approach. Though this way suffers from the thermodynamic inconsistency, the latter was shown to be rather moderate—the order of several percentages at $T \gtrsim 10$ eV [32].

-
- [1] F. Graziani, M. P. Desjarlais, R. Redmer, and S. B. Trickey (Eds.), *Frontiers and Challenges in Warm Dense Matter* (Springer, Heidelberg, 2015).
- [2] D. Marx and J. Hutter, *Ab Initio Molecular Dynamics: Basic Theory and Advanced Methods* (Cambridge University Press, Cambridge, UK, 2009).
- [3] B. Militzer, F. González-Cataldo, S. Zhang, K. P. Driver, and F. Soubiran, *Phys. Rev. E* **103**, 013203 (2021).
- [4] K. P. Driver, F. Soubiran, S. Zhang, and B. Militzer, *High Energy Density Phys.* **23**, 81 (2017).
- [5] D. Ceperley, *J. Stat. Phys.* **63**, 1237 (1991).
- [6] K. P. Driver and B. Militzer, *Phys. Rev. Lett.* **108**, 115502 (2012).
- [7] B. Militzer and K. P. Driver, *Phys. Rev. Lett.* **115**, 176403 (2015).
- [8] D. C. Swift, T. Lockard, R. G. Kraus, L. X. Benedict, P. A. Sterne, M. Bethkenhagen, S. Hamel, and B. I. Bennett, *Phys. Rev. E* **99**, 063210 (2019).
- [9] A. F. Nikiforov, V. G. Novikov, and V. B. Uvarov, *Quantum-statistical Models of Hot Dense Matter: Methods for Computation Opacity and Equation of State* (Birkhauser, Basel, 2005).
- [10] T. Blenski, R. Piron, C. Caizergues, and B. Cichocki, *High Energy Density Phys.* **9**, 687 (2013).
- [11] R. D. Cowan and J. Ashkin, *Phys. Rev.* **105**, 144 (1957).
- [12] N. N. Kalitkin, *J. Exptl. Theor. Phys. (U.S.S.R.)* **38**, 1534 (1960) [*Sov. Phys. JETP* **11**, 1106 (1960)].
- [13] B. F. Rozsnyai, *Phys. Rev. A* **5**, 1137 (1972).
- [14] R. M. More, *Phys. Rev. A* **19**, 1234 (1979).
- [15] D. A. Liberman, *Phys. Rev. B* **20**, 4981 (1979).
- [16] C. Blancard and G. Faussurier, *Phys. Rev. E* **69**, 016409 (2004).
- [17] B. Wilson, V. Sonnad, P. Sterne, and W. Isaacs, *J. Quant. Spectrosc. Radiat. Transf.* **99**, 658 (2006).
- [18] M. Pénicaud, *J. Phys.: Condens. Matter* **21**, 095409 (2009).
- [19] G. Faussurier, C. Blancard, P. Cosse, and P. Renaudin, *Phys. Plasmas* **17**, 052707 (2010).
- [20] V. S. Vorob'ev, A. S. Grushin, and V. G. Novikov, *J. Chem. Phys.* **137**, 031102 (2012).
- [21] C. E. Starrett and D. Saumon, *Phys. Rev. E* **87**, 013104 (2013).
- [22] C. E. Starrett and D. Saumon, *High Energy Density Phys.* **10**, 35 (2014).
- [23] N. Wetta, J.-C. Pain, and O. Heuzé, *Phys. Rev. E* **98**, 033205 (2018).
- [24] N. Wetta and J.-C. Pain, *Phys. Rev. B* **100**, 205127 (2019).
- [25] M. A. Kadatskiy and K. V. Khishchenko, *Phys. Plasmas* **25**, 112701 (2018).
- [26] R. M. More, K. H. Warren, D. A. Young, and G. B. Zimmerman, *Phys. Fluids* **31**, 3059 (1988).
- [27] D. A. Liberman and B. I. Bennett, *Phys. Rev. B* **42**, 2475 (1990).
- [28] F. Lambert, J. Clerouin, and G. Zerah, *Phys. Rev. E* **73**, 016403 (2006).
- [29] D. Sheppard, J. D. Kress, S. Crockett, L. A. Collins, and M. P. Desjarlais, *Phys. Rev. E* **90**, 063314 (2014).

- [30] C. E. Starrett, *Phys. Rev. E* **96**, 013206 (2017).
- [31] C. E. Starrett, J. Daligault, and D. Saumon, *Phys. Rev. E* **91**, 013104 (2015).
- [32] C. E. Starrett and D. Saumon, *Phys. Rev. E* **93**, 063206 (2016).
- [33] J. P. Hansen, *Phys. Rev. A* **8**, 3096 (1973).
- [34] N. F. Carnahan and K. E. Starling, *J. Chem. Phys.* **51**, 635 (1969).
- [35] R. Palmer and J. Weeks, *J. Chem. Phys.* **58**, 4171 (1973).
- [36] N. V. Brilliantov, V. V. Malinin, and R. R. Netz, *Eur. Phys. J. D* **18**, 339 (2002).
- [37] Hartree atomic units $\hbar = m_e = e = 1$ are used throughout the paper.
- [38] Nonadditivity of contributions from the Coulomb interaction and the finite-ion-size effect [36] is not addressed here.
- [39] A direct calculation of thermodynamic functions on the base of the Starrett and Saumon model appears to be not well justified (see Appendix of Ref. [48]), thus driving a need for PAMD simulations.
- [40] J. Chihara, *J. Phys.: Condens. Matter* **3**, 8715 (1991).
- [41] R. Piron and T. Blenski, *Phys. Rev. E* **83**, 026403 (2011).
- [42] A. J. MacLeod, *ACM Trans. Math. Soft.* **24**, 1 (1998).
- [43] W. Kohn and L. J. Sham, *Phys. Rev.* **140**, A1133 (1965).
- [44] P. A. Sterne, S. B. Hansen, B. G. Wilson, and W. A. Isaacs, *High Energy Density Phys.* **3**, 278 (2007).
- [45] V. M. Elkin, V. N. Mikhaylov, A. A. Ovechkin, and N. A. Smirnov, *J. Phys.: Condens. Matter* **32**, 435403 (2020).
- [46] R. M. More, *Adv. At. Mol. Phys.* **21**, 305 (1985).
- [47] F. A. Sapozhnikov, V. V. Dremov, G. V. Ionov, I. V. Derbenev, and N. E. Chizhkova, *EPJ Web Conf.* **10**, 00017 (2010).
- [48] A. A. Ovechkin, P. A. Loboda, and A. L. Falkov, *High Energy Density Phys.* **30**, 29 (2019).
- [49] A. A. Ovechkin, P. A. Loboda, V. G. Novikov, A. S. Grushin, and A. D. Solomyannaya, *High Energy Density Phys.* **13**, 20 (2014).
- [50] A. A. Ovechkin, P. A. Loboda, and A. L. Falkov, *High Energy Density Phys.* **20**, 38 (2016).
- [51] C. E. Starrett and D. Saumon, *Phys. Rev. E* **92**, 033101 (2015).
- [52] Since the OCP corrections to pressure and internal energy are weakly dependent on the mean ion charge, Figs. 5–9 present the OCP data only with $Z_0 = Z_{\text{wkb}}$.
- [53] L. X. Benedict, K. P. Driver, S. Hamel, B. Militzer, T. Qi, A. A. Correa, A. Saul, and E. Schwegler, *Phys. Rev. B* **89**, 224109 (2014).
- [54] One should remember that the PAMD approach provides incomplete account of the finite-ion-size effects: The latter ones are automatically included in the calculation of thermodynamic functions [through the bound-electron density distribution $n_{e,b}(r)$ in $n_e^{\text{PA}}(r)$ (8)] but missing at the stage of interionic potential determination.
- [55] J.-C. Pain, *Phys. Lett. A* **362**, 120 (2007).
- [56] F. Lambert, J. Clerouin, J.-F. Danel, L. Kazandjian, and G. Zerah, *Phys. Rev. E* **77**, 026402 (2008).
- [57] J.-F. Danel, L. Kazandjian, and G. Zerah, *Phys. Rev. E* **79**, 066408 (2009).
- [58] J.-C. Pain and T. Blenski, *J. Quant. Spectrosc. Radiat. Transfer* **81**, 355 (2003).
- [59] J.-F. Danel and L. Kazandjian, *Phys. Rev. E* **91**, 013103 (2015).
- [60] M. D. Knudson and M. P. Desjarlais, *Phys. Rev. Lett.* **103**, 225501 (2009).
- [61] M. D. Knudson and M. P. Desjarlais, *Phys. Rev. B* **88**, 184107 (2013).
- [62] M. C. Marshall, A. E. Lazicki, D. Erskine, R. A. London, D. E. Fratanduono, P. M. Celliers, J. H. Eggert, F. Coppari, D. C. Swift, P. A. Sterne, H. D. Whitley, and J. Nilsen, *Phys. Rev. B* **99**, 174101 (2019).
- [63] M. P. Desjarlais, M. D. Knudson, and K. R. Cochrane, *J. Appl. Phys.* **122**, 035903 (2017).
- [64] Such value of the ratio $\Delta P_i^{\text{OCP}}/(\rho \Delta E_i^{\text{OCP}})$ stems from the virial theorem.
- [65] C. E. Starrett and N. Shaffer, *Phys. Rev. E* **102**, 043211 (2020).
- [66] G. V. Sin'ko, N. A. Smirnov, A. A. Ovechkin, P. R. Levashov, and K. V. Khishchenko, *High Energy Density Phys.* **9**, 309 (2013).
- [67] A. F. Nikiforov, V. G. Novikov, and V. B. Uvarov, *Voprosy atomnoi nauki i tekhniki, Ser.: Metodiki i Programmy* **4**, 16 (1979).
- [68] F. Perrot, *Phys. Rev. A* **20**, 586 (1979).
- [69] U. Gupta and A. K. Rajagopal, *Phys. Rev. A* **21**, 2064 (1980).
- [70] B. Horovitz and R. Thieberger, *Physica* **71**, 99 (1974).
- [71] R. Feynman, N. Metropolis, and E. Teller, *Phys. Rev.* **75**, 1561 (1949).
- [72] T. Blenski and B. Cichocki, *Phys. Rev. E* **75**, 056402 (2007).
- [73] A. I. Voropinov, G. M. Gandel'man, and V. G. Podval'ny, *Sov. Phys. Usp.* **13**, 56 (1970).
- [74] V. G. Novikov and A. A. Ovechkin, Pressure calculations in INFERN0 model, Preprint of the Keldysh Institute of Applied Mathematics, No. 77 (2009), <https://library.keldysh.ru/preprint.asp?id=2009-77>.
- [75] G. Faussurier and C. Blancard, *Phys. Rev. E* **99**, 053201 (2019).